RSC Sustainability

ROYAL SOCIETY OF CHEMISTRY

PAPER

View Article Online
View Journal | View Issue

Cite this: *RSC Sustainability*, 2026, **4**, 493

Systematic study of electrochemical performance of nickel iron hydroxide ($NiFe(OH)_2$) electrocatalyst at high current densities in alkaline seawater solutions

Jack Corbin,[a] Cheng Lyu,[a] David Trudgeon,[a] Mikey Jones,[a] Adeline Loh,[a] Arthur Graf,[bc] Zhenyu Zhang,[a] Jianyun Cao,[d] Ida Nawrocka[a] and Xiaohong Li *[a]

Renewable energy for green hydrogen production presents a promising avenue for sustainable energy storage. However, the increasing demand for green hydrogen may strain freshwater resources. The direct electrolysis of seawater is considered an alternative, but high anion concentration in seawater poses challenges. This study focuses on testing cost-effective electrocatalysts for the oxygen evolution reaction (OER) to facilitate hydrogen generation from seawater electrolysis. The investigation of electrodeposited nickel-iron hydroxide ($NiFe(OH)_2$) on a microelectrode in alkaline seawater solutions shows promising results for achieving low overpotentials at high current densities. In alkaline simulated seawater (1 M KOH and 0.5 M NaCl), the electrode exhibited low overpotentials of 278 and 305 mV at 333 K, to reach current densities of 500 and 1000 mA cm^{-2}, respectively. Furthermore, in alkaline natural seawater, the electrode exhibited low overpotentials of 347 and 382 mV at 333 K, to reach 500 and 1000 mA cm^{-2}, respectively. To deliver a current density of 2000 mA cm^{-2}, the catalyst requires overpotentials of only 341 mV in 1 M KOH and 0.5 M NaCl solution and 409 mV in alkaline Absolute Ocean, a standardised seawater solution. Overall, the findings from this study provide a benchmark to contribute to the understanding of an effective, low-cost, easy-to-synthesize OER catalyst for seawater electrolysis, offering a practical solution for hydrogen generation.

Received 5th August 2025
Accepted 15th November 2025

DOI: 10.1039/d5su00650c

rsc.li/rscsus

Sustainability spotlight

This work outlines a systematic approach to tackle anionic challenges in direct seawater electrolysis using earth-abundant OER electrocatalysts. It supports SDG 7 (Affordable and Clean Energy) and SDG 13 (Climate Action) by demonstrating a sustainable, low-cost $NiFe(OH)_2$ electrocatalyst for oxygen evolution in direct seawater electrolysis. The catalyst performs effectively in saline electrolytes, delivering high current densities with low overpotentials, without dependence on scarce or toxic elements. By enabling clean hydrogen generation from abundant seawater, this research promotes scalable green energy solutions. The updated kinetic model for high-temperature operation further increases industrial relevance. Future enhancements to improve selectivity and durability can amplify its environmental benefits, in line with global efforts to decarbonise energy systems and transition towards a circular, resource-efficient economy.

1 Introduction

The intermittent nature of renewable energy challenges grid stability, requiring an effective energy storage system to balance supply and demand. Hydrogen is a promising storage option, though current production relies on fossil fuels. For green hydrogen production to serve as a possible solution for energy storage and to mitigate greenhouse gas emissions, promoting a cleaner, more resilient energy future, the costs must be reduced.[1,2] Specifically, instead of using expensive noble metal catalysts, affordable catalysts for oxygen evolution reaction (OER) and hydrogen evolution reaction (HER) are required. Significant progress has been made in developing low-cost and efficient electrocatalysts, particularly for the OER. Catalyst developments using first-row transition metals, such as nickel (Ni), iron (Fe), manganese and cobalt-based alloys, have begun to compete with precious metal-based materials such as platinum (Pt), palladium and iridium, which has aimed to mitigate

[a]*Renewable Energy Group, Department of Engineering, Faculty of Environment, Science and Economy, University of Exeter, Penryn Campus, Cornwall TR10 9FE, UK*
[b]*HarwellXPS, Research Complex at Harwell, Rutherford Appleton Lab, Didcot OX11 0FA, UK*
[c]*School of Chemistry, Cardiff University, Main Building, Park Place, Cardiff, CF10 3AT, UK*
[d]*Yunnan Key Laboratory of Electromagnetic Materials and Devices, National Centre for International Research on Photoelectric and Energy Materials, School of Materials and Energy, Yunnan University, China. E-mail: X.Li@exeter.ac.uk*

the inherently sluggish reaction kinetics of the OER due to the 4-electron pathway.

Significant purified freshwater is needed for electrolyte production, even with improved electrocatalysts. As electrolysis becomes mainstream for hydrogen, which can store large amounts of energy, freshwater shortages could pose challenges. Earth's water is 3% freshwater and 97% seawater. Using seawater directly for water splitting is promising, despite some issues, especially with the anodic reaction.

The high chloride (Cl^-) concentration ($\approx$0.5 mol dm^{-3} or 55% of total salt content) (Table S2) in seawater can cause unwanted side reactions at the anode, producing either chlorine (Cl_2) or hypochlorite (ClO^-) in acidic or alkaline environments, respectively, in what is known as the chlorine evolution reaction (ClER), which can compete with the OER, resulting in reduced oxygen production, lower purity of the anode product, and more importantly the generation of highly hazardous by-products. The greatest challenge of seawater electrolysis is to suppress these side reactions to optimise the efficiency of the electrolysis process, improve the overall stability and minimise the environmental impact.[3–5]

Therefore, a stable, affordable, and abundant anode material that can selectively perform the OER over ClOR is in high demand.[6] Among affordable and non-precious metal electrocatalysts, the first-row transition metals, such as Ni, Fe, Mn, and Co, demonstrate great OER activity in alkaline environments on top of their low cost and natural abundance. Specifically, Ni, Fe and stainless steel have been used as metal electrodes in industrial alkaline water electrolysis applications.[7,8] Various metal oxide compounds have recently been created to optimise corrosion prevention and improve OER performance in seawater electrolytes by exploiting the synergistic effect of different metal species.[4,6,9–12] Ni-based materials are well known for reducing the OER overpotential. They are highly corrosion-resistant in alkaline solutions due to forming a stable and protective oxide layer on the surface.[4,13] The importance of Fe in enhancing intrinsic activity is well-known.[14–16] However, there is ongoing discussion regarding the specific impact of Fe on OER kinetics.[8,17] As some authors argue, the inclusion of Fe is believed to enhance the catalyst film conductivity of Ni and Co metal oxides.[17,18] While other authors attribute the heightened OER activity to the presence of the Fe active site.[17] Additionally, when combined with Ni, it improves Ni^{3+} oxidation due to the high Lewis acidity of Fe^{3+}.[8,19–21] The collaborative effect of Ni and Fe together is responsible for the superior OER activity observed, as opposed to pure Ni or Fe oxide.[17,22–24] Generally, studies have confirmed combining Ni and Fe significantly improves OER kinetics and that utilising this effect by the metals is vital to creating a highly active OER electrocatalyst.[17,25–30] Recently, Liang *et al.* synthesised a core–shell catalyst made of NiFe alloy (core) on a Ni foam substrate and ultrathin amorphous NiFe oxyhydroxide (shell) nanowire arrays. This catalyst has shown exceptional OER activity with extremely low overpotentials of 248 and 258 mV required to achieve large current densities of 500 and 1000 mA cm^{-2}, respectively, in an alkaline seawater electrolyte.[31] Haq *et al.* synthesised a novel structure of graphitic carbon nitride-supported Ni-iron oxide (NiO_x–FeO_x@g-C_3N_4); 380 mV overpotential was required to achieve a current density of 1000 mA cm^{-2}, with sustained performance for more than 100 hours in 1 M KOH + seawater at ambient temperature while the formation of hypochlorite was suppressed.[32] However, the synthesis of this catalyst is not economically feasible for large-scale applications due to its multistep procedure, which is conducted over a long time and at high temperatures. Little attention has been paid to the energy and time required for catalyst synthesis, which are essential factors alongside catalytic activity.

To address these key challenges, this paper aims to explore the OER performance of $NiFe(OH)_2$ in alkaline seawater solutions using an electrodeposition synthesis and microelectrode (ME) at current densities $\geq$1000 mA cm^{-2}. The research uses the operational design criterion with limited overpotential based on the principles outlined above, utilising alkaline environments to exploit the overpotential difference between the two electrochemical processes (OER *vs.* ClOR). Considering that saline water is a non-buffered electrolyte, an additive is necessary to prevent changes in the pH during electrolysis; typically, a 1 M concentration of potassium hydroxide (KOH) is used. The paper adds novelty to the research by implementing a microelectrode setup to fabricate $NiFe(OH)_2$ through cathodic electrodeposition while thoroughly testing and comparing the catalyst in a range of saline electrolytes. The microelectrodes uses a microscopic surface area to reach high current densities at very small currents; with a low current of 19.6 μA achieving a current density of 1000 mA cm^{-2} on an electrode diameter of 50 μm, for example, minimising ohmic resistance and mass transfer losses, enabling a focus on catalyst activity. The focus of this study was to implement an efficient OER catalyst in the seawater electrolysis research area that is simple to synthesise using affordable materials and that can achieve high current densities exceeding 1000 mA cm^{-2}, representative of industrial requirements while operating under the known 480 mV threshold and alkaline design criterion to mitigate ClOR.[33] Given the current direction of the literature, with growing interest in abundant materials, this catalyst can act as a benchmark for further modification techniques such as metallic dopants, electrostatic repulsion, outer layer protection and ion-selective layers.[4] This study provides valuable insight into how $NiFe(OH)_2$ operates in a range of seawater electrolytes.

2 Experimental details

2.1. Materials and chemicals

Materials used for synthesis and electrochemical measurements are as follows: Ni microelectrode serving as the working electrode (WE) was fabricated using Ni wire (dia. 50 μm) sealed in glass (Goodfellow, purity 99.0%), providing an active surface area of $\sim 1.963 \times 10^{-5}$ cm^2, a platinum (Pt) microelectrode using Pt wire (dia. 25 μm) sealed in glass (Goodfellow, purity 99.0%), providing an active surface area of $\sim 4.909 \times 10^{-6}$ cm^2. Here is the list of other materials: polished carbon plates (SGL Carbon Bipolar Plates, FR18), KOH (≥90% purity), sodium chloride, NaCl (≥99% purity), isopropyl alcohol, C_3H_8O (≥99.5% purity), hydrochloric acid, HCl (36.5–38.0% purity),

iron(II) sulphate heptahydrate, $FeSO_4 \cdot 7H_2O$ (≥99% purity), Ni(II) sulphate hexahydrate, $NiSO_4 \cdot 6H_2O$ (≥98% purity), ammonium sulphate, $(NH_4)_2SO_4$ (≥99% purity), reference electrode (RE) (Hg/HgO (fabricated in-house) in alkaline electrolytes) and (Ag/AgCl in acidic electrolytes), and Pt mesh counter electrode (CE). All chemicals were purchased from Sigma-Aldrich.

Deionised water (DI) from an Elga Biopure 600 water processor (conductivity < 30 μS cm^{-1}) was used to prepare all aqueous solutions. All chemicals were used as received. A simple mechanical filtration system was used to pass the collected seawater through Whatman® filter paper, Grade 201, with a pore size of 7–14 μm. Conductivity measurements were conducted at 293 K using a Jenway 4520 conductivity meter.

2.2. Synthesis of $NiFe(OH)_2$

For the electrodeposition of the material, we applied a three-electrode setup consisting of a Ni microelectrode ($\varnothing$ = 50 μm) serving as the working electrode, Ag/AgCl in 3 M NaCl as reference electrodes for electrodeposition and a Pt mesh as counter electrode. A small, jacketed glass cell with an approximate volume of 20 mL was used. To prepare the electrodeposition solution, an 18 mM mixed metal sulphate combination with a Ni : Fe molar ratio of 4 : 1 was used. A new solution was prepared for every deposition to avoid the precipitation of Fe_2O_3 due to Fe^{2+} oxidation. The electrodeposition of $NiFe(OH)_2$ was conducted using chronopotentiometry (CP), with a Biologic Potentiostat (Biologic SP-150) and EC-lab software. CP was conducted at a constant cathodic current density of −250 mA cm^{-2} for 50 seconds at room temperature (293 K) on the microelectrode; a constant current density of 25 mA cm^{-2} for 500 seconds at 293 K was used for larger surface area substrates such as Ni foil and carbon plate. On larger surface area substrates, a magnetic stirrer was added to the solution and stirred at 500 rpm to improve the mass transport of deposition. The pH of the deposition solution was adjusted to ∼4 (±0.1) using 1 M HCl to avoid the precipitation of species such as Fe_2O_3 and $Fe(OH)_3$ in the solution. Following the electrodeposition process, the microelectrode was removed from the cell, and the tip was rinsed thoroughly with DI water. The electrolyte consisted of $NiSO_4$ and $FeSO_4$, which served as the sources of Ni and Fe, respectively. $(NH_4)_2SO_4$ is used in the solution to increase the tensile stress and hardness of the deposit.[1] Research has suggested that $(NH_4)_2SO_4$, when used in an optimum ratio (<12 g dm^{-3}), can decrease grain size and slightly improve corrosion resistance.[1,15] However, highly concentrated $(NH_4)_2SO_4$ solutions can increase the stress of a coating, leading to a cracked morphology.[15]

2.3. Electrochemical characterisation

Electrochemical measurements were conducted using a Bio-logic Potentiostat (SP-150) with EC-Lab software (version 11.33) connected in a 3-electrode configuration, consisting of Ni microelectrode as the WE (Fig. S2) with (Hg/HgO) reference electrode (RE) and Pt mesh counter electrode (CE). Linear sweep voltammetry (LSV) and cyclic voltammetry (CV) were used to investigate the OER performance and redox behaviour of the samples, and chronopotentiometry (CP) was used to examine the stability of the samples. A bespoke 20 mL glass cell (Fig. S3) was used for electrochemical testing, with the upward orientation of the microelectrode allowing for efficient removal of bubbles from the surface. The microelectrode was inserted into the cell setup for electrochemical testing in different electrolytes: 1 M KOH, 1 M KOH & 0.5 M NaCl, and 1 M KOH & seawater. CV was conducted between 0.1 V to 0.65 V (*vs.* Hg/HgO) with a scan rate of 100 mV s^{-1} and later converted to RHE. LSVs were collected using a potential range of 1.224 to 1.624 V (*vs.* RHE) with a scan rate of 1 mV s^{-1} to reach steady-state conditions. Testing was conducted at 293 K and elevated temperatures (333 K). A Grant TC120 water bath was used to control the water jacket temperature. Measured potentials were converted to the reversible hydrogen electrode (RHE) using eqn (S8).

2.4. Physical characterisation of materials

Scanning electron microscopy (SEM, FEI Quanta FEG 650) was used to investigate the catalyst's morphology on each point of the electrode. The materials' composition was examined using Energy Dispersive X-ray Spectroscopy (EDS, TESCAN VEGA3 GMU SEM with Oxford instruments X-Max 80 mm^2 energy dispersive X-ray spectrometer). The $NiFe(OH)_2$ samples were prepared on polished carbon plates to avoid the influence of Ni substrate for EDS analysis. The electrode was masked with non-conductive tape to control the substrate surface area to 1 cm^2. The samples were then washed with DI water and dried before characterisation. X-ray diffraction (XRD) (Bruker D8, Cu-Kα X-ray source with wavelength λ = 1.5418 Å) was carried out between angles of 10–90° in increments of 0.02° to study the crystal structure of the materials. Transmission electron microscopy (TEM) (JEOL 2100 with Oxford instruments X-Max 80 mm^2 energy dispersive X-ray spectrometer) was used to examine the materials' morphology, crystal structure and composition. The sample was prepared using chronopotentiometry, deposited onto a polished carbon plate, exfoliated from the substrate with a spatula, crushed, and dispersed in isopropanol under ultrasonic vibration for 15 minutes. After settling, a drop of liquid containing nanoparticles was added to a holey-carbon-coated copper grid and air-dried. The dried grid with the sample on top was then characterised using TEM. The ImageJ software suite was used to analyse the selected area electron diffraction (SAED) data. X-ray photoelectron spectroscopy (XPS) data was acquired at the HarwellXPS National Facility. XPS data was acquired using a Kratos Axis SUPRA using monochromatic. Al Kα (1486.69 eV) X-rays at 15 mA emission and 12 kV HT (180 W) and a spot size/analysis area of 700 × 300 μm. Survey spectra were obtained using a pass energy of 160 eV. Charge neutralisation was achieved using an electron flood gun with filament current = 0.4 A, charge balance = 2 V, filament bias = 4.2 V. Successful neutralisation was adjudged by analysing the C 1s region wherein a sharp peak with no lower BE structure was obtained. Spectra have been charge-corrected to the main line of the carbon 1s spectrum (adventitious carbon) set to 284.8 eV. All data was

recorded at a base pressure of below 9×10^{-9} Torr and a room temperature of 293 K. Data was analysed using CasaXPS v2.3.19PR1.0. Peaks were fit with a Shirley background before component analysis. The chemical structures of the samples were examined using confocal Raman spectroscopy (WITec Alpha-300R) at a wavelength of 532 nm.

3 Results and discussion

3.1. Proposed electrodeposition process of $NiFe(OH)_2$

The deposition process uses widely researched and accepted mechanisms.[34–36] Numerous studies on Ni deposition have been conducted, and different mechanisms have been proposed. Wiart *et al.*, Bockris *et al.* and later Proud and Müller propose the most relevant studies for this deposition.[34,36,37] The adsorption process involves an intermediate of Ni monohydroxide ($Ni(OH)^+$). The adsorbing species depends on pH and proceeds more rapidly in pH 5 than in pH 3 systems.[34,35] The deposition process is given for Ni for simplicity, but Bockris *et al.* propose that Fe deposits *via* a similar mechanism.[36,37] The Ni and Fe present in the solution are divalent, positively charged ions (Ni^{2+} and Fe^{2+}) that react with 2 electrons.[38]

$$Ni(OH)^+ \rightarrow Ni(OH)_{ads}{}^+ \quad (1)$$

$$Ni(OH)_{ads}{}^+ + e^- \rightarrow Ni(OH)_{ads} \quad (2)$$

An overall reaction is thus considered (eqn (1)) for initiating the deposition process, but the process is suggested to proceed by eqn (1)–(4).[36] The $Ni(OH)_{ads}$ forms a foundation for which the deposition of Ni can occur (eqn (3) and (4)).

$$Ni(OH)_{ads}{}^+ + Ni^{2+} + 2e^- \rightarrow Ni + Ni(OH)_{ads} \quad (3)$$

$$Ni(OH)_{ads} + e^- \rightarrow Ni + OH^- \quad (4)$$

Protons are discharged during the deposition, eventually leading to the HER. The process initiates *via* eqn (5)–(7):

$$H^+ + e^- \rightarrow H_{ads} \quad (5)$$

$$2H_{ads} \rightarrow H_2 \quad (6)$$

$$Ni(OH)_{ads}{}^+ + H_{ads} + e^- \rightarrow Ni + H_{incl} + OH^- \quad (7)$$

The H_{ads} is responsible for the passivation seen at lower potentials. It is hypothesised that as the potential increases as a result of the 250 mA cm^{-2} current density used, the potential will continue to increase more negatively (Fig. S4), and the dominant reaction will become the water reduction, producing further hydrogen-containing forms of Ni (eqn (7)), raising the pH in the diffusion layer.[35] Only a slight pH change is needed to produce Ni hydroxide at a higher pH, which could provide evidence for producing quantities of $NiFe(OH)_2$.[34,39]

As the final part of the deposition proceeds, the overpotential decreases due to the surface area increasing with the deposition of the catalyst on the microelectrode tip surface, meaning that the unit area effective current density decreases over the period. It is further reported in the literature that a second passivation process could occur simultaneously *via* the precipitation of a passivating coverage of hydroxylated Ni species (eqn (8)).[34,36,37]

$$Ni^{2+} + 2OH^- \rightarrow Ni(OH)_2 \quad (8)$$

$$Ni(OH)_2 + 2e^- \rightarrow Ni + 2OH^- \quad (9)$$

This passivation is partially disrupted due to the relative acceleration of competing processes or the reaction's potential dependence (eqn (9)). Consequently, based on well-established mechanisms, the surface is proposed to consist of a combination of metallic Ni and Fe (Ni^0 and Fe^0) alongside hydroxylated Ni and Fe species.[34] Nevertheless, surface hydroxides readily form in an alkaline environment, leading to the designation of $NiFe(OH)_2$.

The electrodeposition bath concentration also significantly impacts the material deposited. Our previous work found an optimal ratio of Ni : Fe (4 : 1) for $NiFe(OH)_2$ deposition.[28,29] This study applies this further since the performance of different ratios has already been well-studied.[28,29] EDS analysis (Fig. S5) shows a ratio of 83.9% Ni to 16.1% Fe, close to the deposition solution ratio. Previous research has demonstrated that introducing a small quantity of Fe to Ni can improve the rate and activity of OER. However, when Fe outweighs the Ni contribution, it can have the opposite effect and hinder OER performance.[17,25–30] Dong *et al.* have supported this observation, confirming that when Fe content surpasses Ni, the catalyst is inferior to pure Ni alone.[4,14,29]

3.2. Material characterisation

SEM was used to investigate the catalyst morphology under different deposition current densities. Using current density as high as 250 mA cm^{-2} (Fig. 1b) during electrodeposition means the potential will reach a value greater than the standard reduction potential of water (1.23 V). As a result, a proportion of H_2 will be produced, reducing the current efficiency.[40] Higher current densities will initiate a growth rate where mass transfer is limiting, creating larger groups of deposits on the substrate due to an increasing nucleation rate and the influence of further electrochemical reactions (*i.e.* HER) becoming more dominant.[40,41] To illustrate this, lower current densities were used to synthesise $NiFe(OH)_2$, specifically, 2.5 mA cm^{-2} (Fig. 1c) and 25 mA cm^{-2} (Fig. 1d), while increasing the deposition period to maintain the catalyst's capacity. The deposit produced with the lower current density (Fig. 1b) demonstrates a much smoother morphology; the particles are more evenly distributed. Increasing the current density by a factor of 10 (Fig. 1c) demonstrates that the nucleation rate has risen. This is evident as the deposited particles are larger and there is a greater clustering of deposits due to the increased number of particles being deposited.[41]

EDS analysis of catalyst deposited on polished carbon plates (Fig. 1e–g) revealed a uniform distribution of Ni and Fe across the substrate. The influence of current density on electrodeposition has impacted the ratio of Ni and Fe differently. At 250 mA cm^{-2} (Fig. S5), the deposit is 83.9% Ni and 16.1% Fe, which could result from the large clusters of particles, leaving more

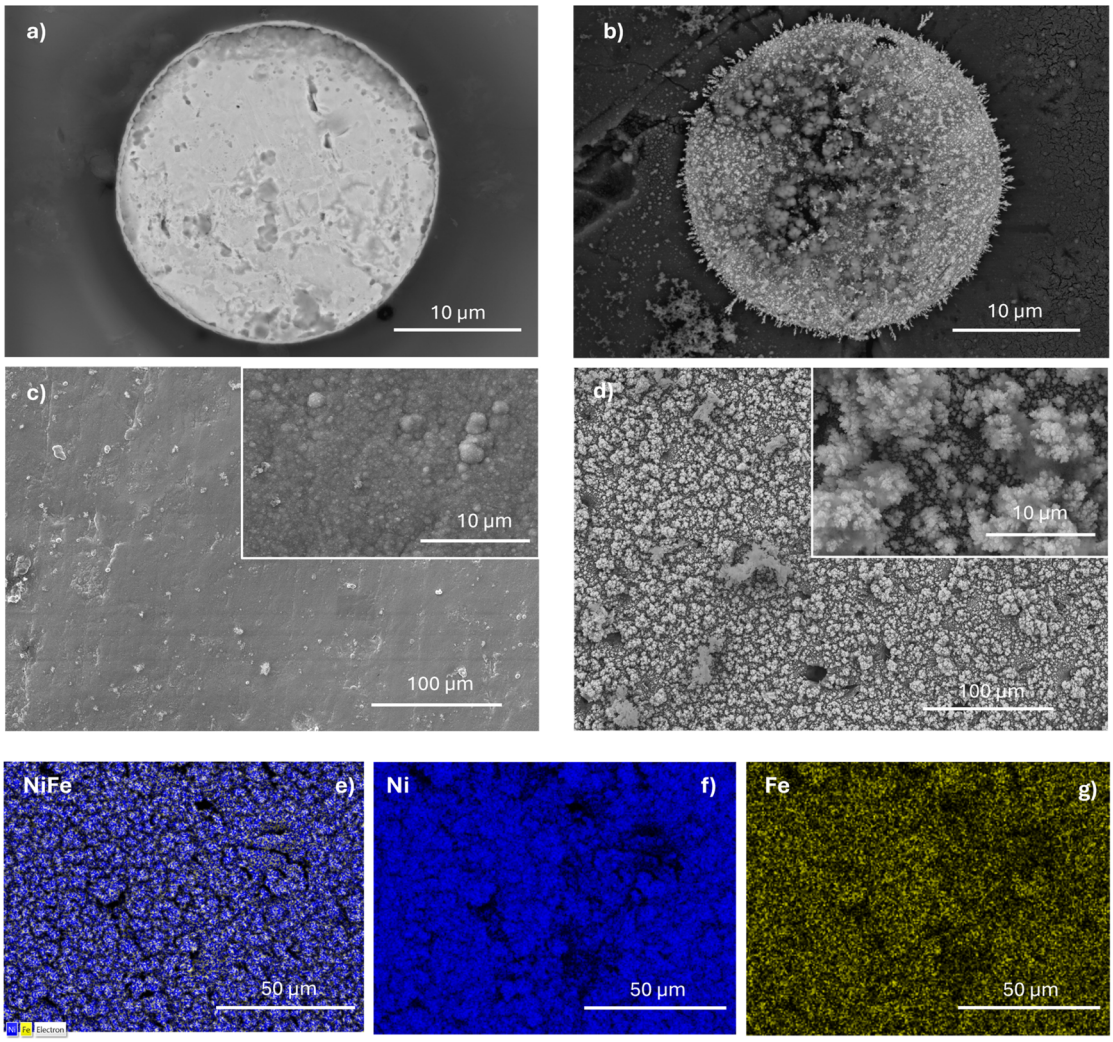

Fig. 1 (a) SEM image of polished uncoated/pristine nickel microelectrode. SEM images of varied electrodeposition capacities within 18 mM metal sulphate & 25 mM ammonium sulphate (b) SEM image of $NiFe(OH)_2$ coated Pt microelectrode, using 250 mA cm^{-2} for 50 seconds under low vacuum of SEM chamber to avoid charging effects (c) high vacuum SEM image of 2.5 mA cm^{-2} for 5000 seconds on Ni foil, 1 cm^2 surface area (d) high vacuum SEM image of 25 mA cm^{-2} for 500 seconds on Ni foil, 1 cm^2 surface area (e) EDS map of $NiFe(OH)_2$ catalyst synthesised using 25 mA cm^{-2} for 500 seconds on polished carbon plate, both Ni and iron overlayed showing distribution (f) Ni distribution (g) Fe distribution.

voids, consistent with more rapid production of H_2 bubbles and a greater uncovered substrate surface, distorting the ratio of Ni to Fe.[28] At 25 mA cm^{-2} (Fig. S6), the Ni and Fe ratio averages over the sample to be 80.46% and 19.53%, respectively. At 2.5 mA cm^{-2} (Fig. S7), the Ni to Fe average changes to 74.87% and 25.12%. This trend of a higher Fe content at lower deposition current densities could be attributed to the kinetics of the deposition; specifically, at 250 and 25 mA cm^{-2}, the deposition is more kinetically driven, and Ni, being more electrochemically favoured due to a lower standard electrode potential for (Ni^{2+} to Ni = −0.25 V *vs.* Fe^{2+} to Fe = −0.44 V) deposits preferentially, leading to a higher Ni contribution.[34,42] Further to this, at higher current densities, mass transport limitations occur because metal ions are consumed rapidly at the electrode surface. Ni, present in a higher concentration (80% in solution), gets preferentially reduced.[34,43] In contrast, at 2.5 mA cm^{-2}, the deposition process becomes more controlled by diffusion rather than charge transfer kinetics, meaning that the preferential deposition of Ni over Fe has less impact, and there is little to no effect from HER, both resulting in an increasing Fe content.

XRD analysis was conducted to obtain information on the crystallinity of the electrodeposited sample. Fig. 2d shows distinct diffraction peaks for pure graphite; an intense peak is observed at a 2θ of 26.4°, with a lattice spacing of 0.34 nm (~3.4 Å), which links to the diffraction plane of graphite (002) and also a slight peak is observed at a 2θ of 54.5°, also for graphite at the diffraction plane (004), lattice spacing 0.19 nm (1.9 Å).[44,45] Graphite peaks from the substrate dominate due to its highly crystalline lattice, which initially suggested that the crystallinity of the deposited catalyst was not high enough to be detected and likely meant the catalyst was amorphous. However, some small peaks were encountered even on the graphite substrate, which indicates that the intensity of the graphite peaks made identifying any catalyst peaks difficult. To confirm this, the catalyst was deposited on a Ni substrate and compared to the carbon patterns to examine the Ni peaks at a higher intensity.

The high-intensity peaks of the coated Ni substrate pattern at 44.5° and 52° correlate to metallic Ni (COD 2100646), likely from the metal substrate, with a calculated lattice spacing of 0.21 nm (~2 Å) and ~0.17 nm (1.7 Å), respectively, corresponding to planes of (111) and (200).[46] Metallic Fe (COD 7204904) can be found to overlap with these peaks, hence the broader base of the peak at 52°. Further, observed diffraction peaks at approximately 38°, 64°, 76° and 79° are linked to Ni oxide (NiO) and can be readily indexed to (111), (220), (311) and (222) planes.[47,48] These peaks arise potentially due to surface oxidation during the samples' processing and handling and possibly formed as part of the deposition process.[49] Metallic Ni and NiO both adopt the face-centred cubic (FCC) structure.[47,48] The lack of other distinct peaks in both substrate XRD patterns means no Ni/Fe hydroxide products existed. Since a significant portion of the crystallinity originates from the metallic substrate, we are led to believe the catalyst is largely amorphous but with small crystalline features stemming from a small metallic portion of the deposition.

TEM analysis was conducted to investigate the crystallinity of the deposit further. Fig. 2a and b show the images captured using TEM, and Fig. 2c shows the SAED. The high-magnification TEM image (Fig. 2b) shows a largely amorphous area encompassed by a few short-ranged/nano-meter-sized crystalline areas. Furthermore, some dotted ring patterns were observed in the SAED (Fig. 2c), which was then used to confirm the calculated lattice spacing and the Miller indices from the XRD spectrum. The small crystalline portion of the diffraction pattern corresponds to metallic species; the interplanar *d*-spacing can be calculated from the SAED using Bragg's law and linked to the Bragg angle (eqn (S9)) as approximately 2.0 Å, 1.7 Å and 1.4 Å, which links to the standard diffraction planes of (111), (200) for Ni metal.[48–50] The TEM micrograph in Fig. 2b displays central interconnected crystals with amorphous dendritic structures towards the edge. We believe the catalyst is largely amorphous but has some crystalline features related to the mixed metal deposition due to the reduction of Ni and Fe in the cathodic electrodeposition.

To gain further information on the catalyst bonding, we applied *ex situ* Raman spectroscopy to the samples. Samples were deposited on a carbon plate to avoid any influence from nickel foam (NF). Fig. S8 highlights spectra taken for each of the electrodeposited catalysts and subsequently overlaid. As described by Dionigi and Strasser, a Raman shift region between

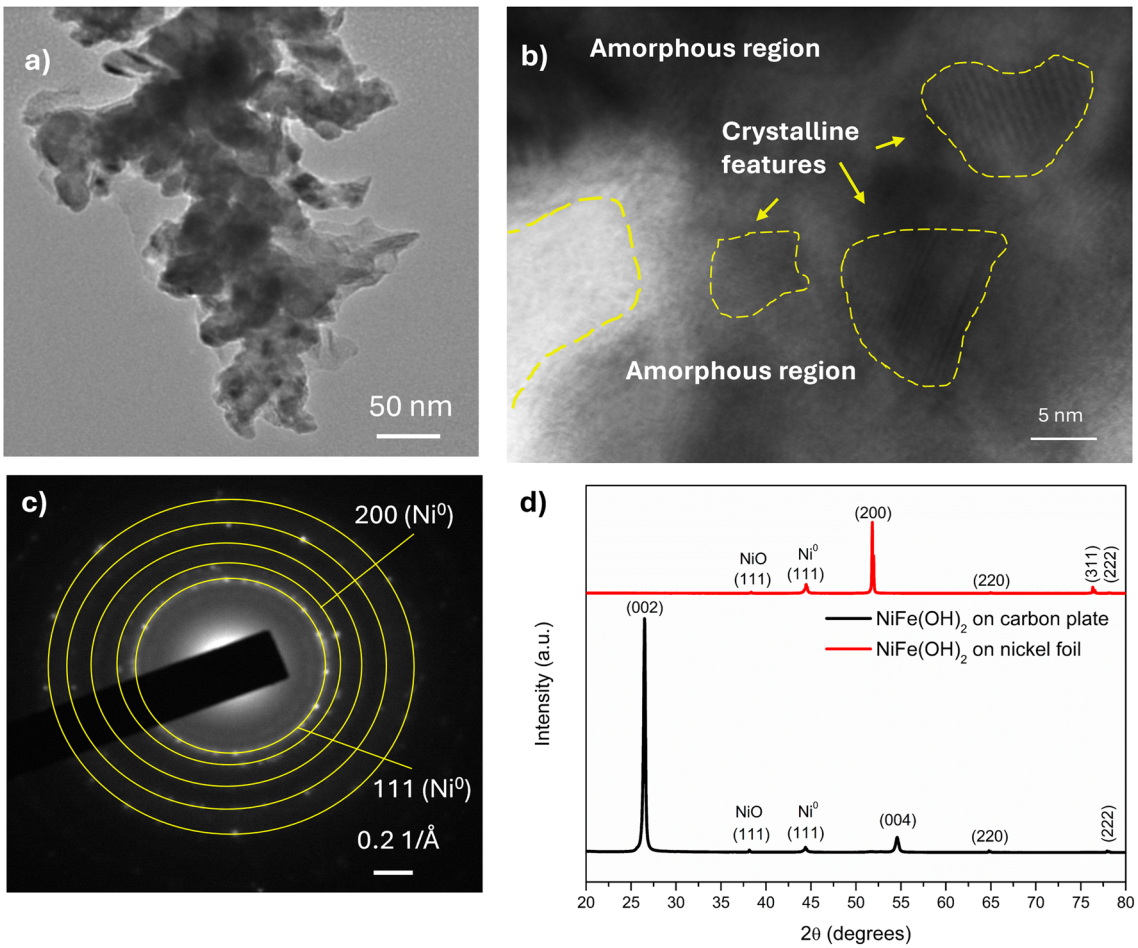

Fig. 2 (a) Low-magnification TEM image of $NiFe(OH)_2$ (b) high-resolution TEM image of $NiFe(OH)_2$ (c) SAED ring diffraction pattern of $NiFe(OH)_2$ with the relevant Miller indices of the two most prominent peaks (d) X-ray diffraction (XRD) patterns for $NiFe(OH)_2$ on a carbon plate substrate and on a Ni foil substrate.

300–800 cm^{-1} is of interest, as it is the region where Ni–O and Ni–OH stretching modes are observed in $Ni(OH)_2$ compounds.[51] $NiFe(OH)_2$ illustrates a broad peak at ~530 cm^{-1}, the broadness of the peak makes it challenging to deconvolute into the defined peaks associated with α & β-$Ni(OH)_2$ in this region. The broadness is characteristic of amorphous electrodeposited materials. In Fig. S8, the broad peak, which is centred around ~530 cm^{-1}, is a distinctive feature of disordered/defective β-$Ni(OH)_2$, commonly reported by other authors.[51–54] Due to the broadness of the peak, it could also have elements of α-$Ni(OH)_2$, typically observed at ~460 cm^{-1}, another form of E-type metal–oxygen vibration. Interestingly, An *et al.* found that increasing Fe content resulted in a decrease in intensity of the 530 cm^{-1} peak and an increased Raman shift, which can be attributed to the shoulder peak in Fig. S8; this is estimated to be influenced by the Fe^{3+}–O–Fe^{3+} structure.[52,54–56] The peaks at higher Raman shifts (~1500 cm^{-1} and 2750 cm^{-1}) are associated with ordered graphite, stemming from the carbon plate substrate.[57]

3.3. XPS data & analysis

To further gain information on the electrodeposition mechanism, including the confirmation of metal hydroxides and degradation from seawater electrolysis, XPS analysis of the oxidation states and composition of elements was conducted (Fig. 3). Samples were prepared on a polished carbon plate, and all XPS data were calibrated using the adventitious carbon peak at 284.8 eV to compensate for charge build-up. Fig. 3a shows the XPS survey scan for $NiFe(OH)_2$.

As established by Biesinger *et al.* for Ni compounds, the spin–orbit splitting of Ni $2p_{3/2}$ and Ni $2p_{1/2}$ is typically large enough, so that only the more intense Ni $2p_{3/2}$ signals need to be analysed.[58] Fitting of the high-resolution Ni $2p_{3/2}$ spectrum (Fig. 3a) shows

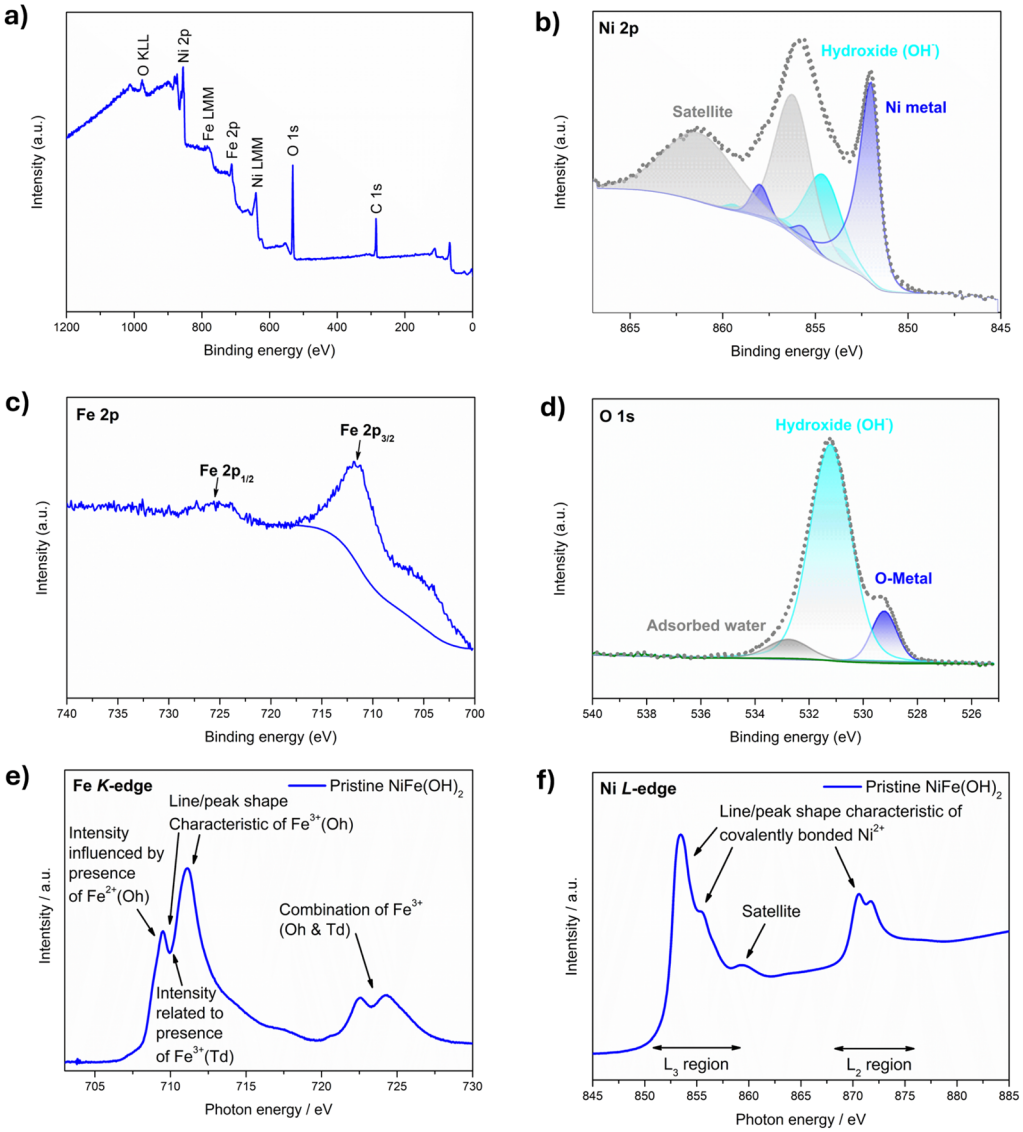

Fig. 3 (a) Survey scan of the XPS spectrum of $NiFe(OH)_2$ obtained on a carbon plate. And fitting results of the high-resolution scans in the (b) Ni 2p region (c) Fe 2p region (d) O 1s region (e) normalised Fe K-edge XANES spectra for $NiFe(OH)_2$ (f) normalised Ni L-edge XANES spectra for $NiFe(OH)_2$.

two distinct oxidation states, with a ratio of 1 : 3 of Ni^0 to Ni^{2+}. Metallic Ni, with the main peak position at 852.5 eV, which matches the core line as stated in the literature.[58,59] Further multiplet splitting (dark blue shaded regions) was used to confirm the status of the Ni metal deposit, and further indicates that the deposition is a combination of Ni compounds and Ni metal.[58] The light blue shaded region indicates further contributions to the Ni $2p_{3/2}$ spectra, corresponding to $Ni(OH)_2$, with a dominant peak at a binding energy of 854.57 eV, and a multiplet at 856 eV, characteristic of Ni^{2+}.[60] The grey shaded regions indicate satellite peaks. For the Fe 2p spectrum (Fig. 3b), analysis is more complicated due to strong overlap with the Ni LMM auger peaks, particularly when using an Al Kα X-ray source.[61,62] Here, we find that the Ni Auger is predominant in the region, alongside Fe 3p and 2s regions, which were also recorded to elucidate information on iron. However, while regions show weak signals, indicating that some iron is located at the surface of the sample, we cannot conclude this as definite due to the overlap. The O 1s spectrum (Fig. 3d) further confirms the Ni 2p region with distinct regions from O-metal (~529 eV), hydroxyl (~531 eV) and adsorbed water (~532.6 eV) with the ratio of the O 1s components of approximately 1.5 : 10 : 1.

As a result, we investigate the electronic and local structures of $NiFe(OH)_2$ using X-ray absorption spectroscopy (XAS), which provides deeper insight into the sample's surface. Fig. 3c displays the Fe K-edge X-ray absorption near-edge structure (XANES) spectra of pristine $NiFe(OH)_2$. The Fe K-edges are between the Fe^{2+} and Fe^{3+}, indicating mixed oxidation states of Fe in the sample, with a sharp rise between 710 and 712 eV, which is typical of Fe^{3+} species (Fe_2O_3).[63,64] Hall *et al.* recently presented similar findings to spectral shapes in Fig. 3c, highlighting that the peak is a combination of Fe^{2+} octahedral (Oh), Fe^{3+} tetrahedral (Td) and Fe^{3+} Oh.[64] The difference in intensity at approximately ~708 eV, between the pre- and main edges of the spectral shape, relates to the presence or absence of Fe^{3+} Td (Fig. 3c).[64] Furthermore, the width of the spectral shape at the main edge (~710 eV) is also influenced by the cation contribution, with narrower features further confirming a lesser presence of Fe^{3+} Td.[64] Quantitative identification of the various Fe species cannot be achieved solely through fitting NEXAFS spectra; supplemental spectral features or additional data are required.

Soft XAS analysis further revealed insight into the surface oxidation state of Ni. The Ni L-edge spectra (Fig. 3d) reinforces the Ni 2p XPS spectra in Fig. 3a. Based on the well-defined line shape in both L_3 and L_2 regions, the environment is more Ni^{2+} dominant, stemming from more covalent, OH^- ligands and from partial Fe substitution in the lattice. Furthermore, it is characteristic of low-spin Ni^{2+} with photon energies (~853 eV and ~871 eV), indicating an oxidation state of Ni^{2+} in octahedral coordination, with a mixed covalency with OH^- ligands, consistent with $Ni(OH)_2$.[65–68]

3.4. Electrochemical characterisation

3.4.1. Electrochemical surface area calculation. This experiment aimed to determine the difference between the

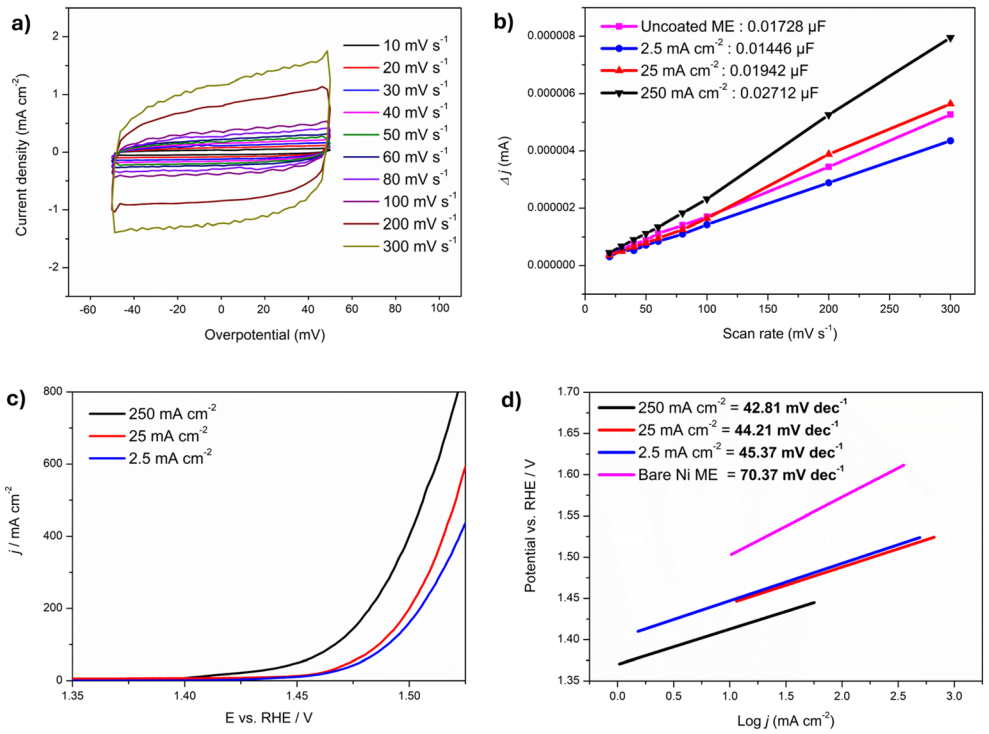

Fig. 4 (a) Example bare 25 μm Ni microelectrode in 1 M KOH at 293 K using CVs at different scan rates to calculate double-layer capacitance (b) average current ($\Delta j = (j_a - j_c)/2$) against the scan rate showing the double-layer capacitance (C_{dl}) extracted from the corresponding CVs of varied synthesis current densities (c) corresponding electrochemical performance of Ni microelectrode synthesised using different electrodeposition current densities in 1 M KOH at 333 K at a scan rate of 1 mV s^{-1} (d) Tafel plot of catalyst coated Ni microelectrode using different electrodeposition current densities, compared to uncoated Ni microelectrode.

electrochemical surface area (ECSA) and roughness factor (R_f) of a pristine Ni microelectrode and a Ni in results emphasise the inaccuracy microelectrode coated with a $NiFe(OH)_2$ catalyst at three different electrodeposition current densities, 2.5, 25 & 250 mA cm^{-2}. The electrochemical surface area (ECSA) was estimated using the double layer capacitance (C_{dl}) method, using cyclic voltammograms (CVs) at 10 potential scan rates between 10 mV s^{-1} and 300 mV s^{-1} within a potential region ±50 mV *vs.* open circuit potential (OCP) in 1 M KOH electrolyte to ensure that no faradaic current occurs.[69] Fig. 4a demonstrates an example of the CVs collected during the 10 potential scan rates on a bare Ni ME. Values for current density were taken at the midpoint of CV scans, and the average current density is plotted against the scan rate in Fig. 3b; the slope of these plots is equal to the C_{dl} of each electrode material. The non-Faradic current density-based ECSA was estimated according to eqn (10):

$$\mathrm{ECSA} = \frac{C_{dl}}{C_s} \tag{10}$$

where C_s is the electrode's specific capacitance, it is typically given as 0.020 mF cm^{-2} in 1 M KOH electrolyte for Ni.[70,71] However, since capacitance is largely affected by the media, plate area and distance between the plates and the dielectric material, a secondary Ni microelectrode with the same diameter was employed as the counter electrode and positioned consistently opposite the working microelectrode (approximately 1 cm gap). This methodology can be used as a normalisation of the C_{dl} on the microelectrode, as the value pertains to the microelectrode rather than being a specific capacitance for Ni itself, the standard C_s value for Ni shouldn't be used here, as it leads to inaccuracies shown in Table 1.

For the bare Ni microelectrode can be taken as the C_s value, which results in a more appropriate ECSA and Roughness factor (R_f) estimation (Table 1). The R_f is calculated by dividing the ECSA by the geometric surface area.

The variations in results emphasise the inaccuracy of using the standard C_s for Ni and the relevance of applying a normalisation methodology. The $NiFe(OH)_2$ coated microelectrode deposited at 250 mA cm^{-2} exhibits a larger ECSA of 7.704×10^{-6} cm^2, compared to 5.517×10^{-4} cm^2 for 25 mA cm^{-2} and 4.108×10^{-6} cm^2 for 2.5 mA cm^{-2}, indicating a 36.28% increase in ECSA from a bare Ni microelectrode to 250 mA cm^{-2} $NiFe(OH)_2$ coated ME. Based on these estimations, the uncoated Ni microelectrode exhibits a larger ECSA than $NiFe(OH)_2$ deposited at 2.5 mA cm^{-2}, as well as a higher R_f (Table 1). Given that the R_f provides an insight into the topography of a catalyst, this could arise from the polishing process of the bare ME, which aims to mitigate irregularities on the surface but is very difficult to create a perfectly flat surface (Fig. 1a). Therefore, applying a smooth catalyst layer, which is achieved at low deposition current densities (Fig. 1c) can result in a smoother morphology than a pristine ME.[40] Further results for R_f reveal larger values for the $NiFe(OH)_2$ coated microelectrode at 250 mA cm^{-2} ($R_f = 1.569$), compared to 25 mA cm^{-2} ($R_f = 1.123$) and an R_f of 0.836 for the 2.5 mA cm^{-2} coated microelectrode; the different morphologies in Fig. 1b–d emphasise this, where the sample deposited at 250 mA cm^{-2} (Fig. 1b) shows a rougher topography than Fig. 1c (25 mA cm^{-2}) and Fig. 1d shows a rougher topography than Fig. 1c (2.5 mA cm^{-2}). Overall, the deposition process has led to an increase in the electrochemical surface area and roughness of the topography at current densities greater than 2.5 mA cm^{-2} compared to an uncoated electrode and reveals the electrochemical benefit of using higher deposition current densities.

3.4.2. Electrochemical performance of varied deposition current densities. Modifications to the deposition period were done so a different substrate could be used. Applying 250 mA to a 1 cm^2 surface area for characterisation analysis creates vigorous gas evolution that can detach parts of the catalyst during the deposition procedure. SEM imaging was carried out to investigate the effect of current density on morphology. The images (Fig. 1c and d) demonstrate that at lower current densities, the particles are much more evenly distributed due to a reduced nucleation rate, and as the deposition current density increases to 250 mA cm^{-2} (Fig. 1b) there is a greater number of grouped deposits. It is this effect that creates a rougher morphology, leading to a higher roughness factor and ECSA. As shown in Fig. 4c, the achieved OER current density is the highest at a synthesis current density of 250 mA cm^{-2}. We assume this reduction in overpotential is attributed to a number of aspects. It is likely to be largely influenced by the increased active surface area from the mixture of large and small deposit particles, which means there are a greater number of active sites. To further investigate this, we plotted the LSVs against the normalised ECSA value in Table 1. Fig. S1 shows the electrochemical performance of each synthesis when the current density is brought much closer together. This confirms our premise that the performance is largely dictated by the roughness of the deposit. EDS analysis has also shown that the lower deposition current density leads to a higher Fe content. As explained previously in the literature, when the Fe content outweighs the Ni, it can lead to reduced electrochemical performance (Fig. S7).[4,14,29] Higher current densities can also result in rougher, more porous deposits as the rapid deposition

Table 1 Methods and values for ECSA of pristine Ni microelectrode and coated Ni ME

Synthesis parameters for $NiFe(OH)_2$ coated microelectrode	C_{dl} (μF)	ECSA calculated using established C_s (20 μF cm^{-2}) for Ni	Roughness factor, R_f	Normalised ECSA calculated using microelectrode C_{dl}	Normalised roughness factor, R_f
Uncoated/pristine	0.01728	8.639×10^{-4} cm^2	175.99	4.909×10^{-6} cm^2	—
2.5 mA cm^{-2} for 5000 s	0.01446	7.23×10^{-4} cm^2	147.28	4.108×10^{-6} cm^2	0.836
25 mA cm^{-2} for 500 s	0.01942	9.71×10^{-4} cm^2	197.79	5.517×10^{-6} cm^2	1.123
250 mA cm^{-2} for 50 s	0.02712	1.356×10^{-3} cm^2	276.22	7.704×10^{-6} cm^2	1.569

doesn't allow for sufficient time for ions to diffuse and organise into stable configurations.[72]

To further confirm the electrochemical performance beyond Fig. 4c, Tafel analysis of the $NiFe(OH)_2$ at varying deposition current densities is shown in Fig. 4d. The slopes were extracted from LSV data. A lower Tafel slope is favourable to catalytic activity and implies a higher attainable current density at a given overpotential. Notably, all electrodeposited samples exhibit similar Tafel slope values between 42 to ~46 mV dec^{-1}, indicating that all samples proceed by a similar OER mechanism.[28] A Tafel slope of ~40 mV dec^{-1} indicates that the second electron transfer step of the OER mechanism is the rate-determining step.[73–75]

3.5. Oxygen evolution of $NiFe(OH)_2$ catalyst in varying electrolytes

3.5.1. 1 M KOH. The electrochemical OER performance of $NiFe(OH)_2$ deposited at 250 mA cm^{-2} was investigated in 1 M KOH as the electrolyte at 293 K and 333 K (Fig. 5a). Higher temperatures are often used in industrial electrolysis applications with large-scale electrolysers such as alkaline water electrolysers (AWE) and proton exchange membrane water electrolysers (PEMWEs).[76–78] In this study, elevated temperatures are used to be representative of industrial conditions.

The electrochemical performance at 333 K surpasses that at room temperature due to enhanced reaction kinetics and improved mass transfer. Specifically, current within an electrolyte is facilitated by moving ions, while resistance is attributed to the limited mobility of these ions. The increase in temperature boosts the kinetics of these ions, thereby reducing resistance and the required potential. This is shown by a noticeable decrease in overpotential, which is observed across all electrolytes, as shown in Fig. 5b and c. At 100 mA cm^{-2} in 1 M KOH, $NiFe(OH)_2$ requires only 256 mV, compared to 307 mV at 293 K.

The LSV curves in Fig. 5a, highlight the increase in catalytic activity from applying the $NiFe(OH)_2$ catalyst to the microelectrode without *iR* compensation. The slope of the catalyst-coated microelectrode polarisation curve is steeper with a lower OER onset potential at approximately ~1.44 V *vs.* ~1.52 V for the pristine ME, with a ~80 mV reduction. The onset OER potential is defined in this study as the potential corresponding to

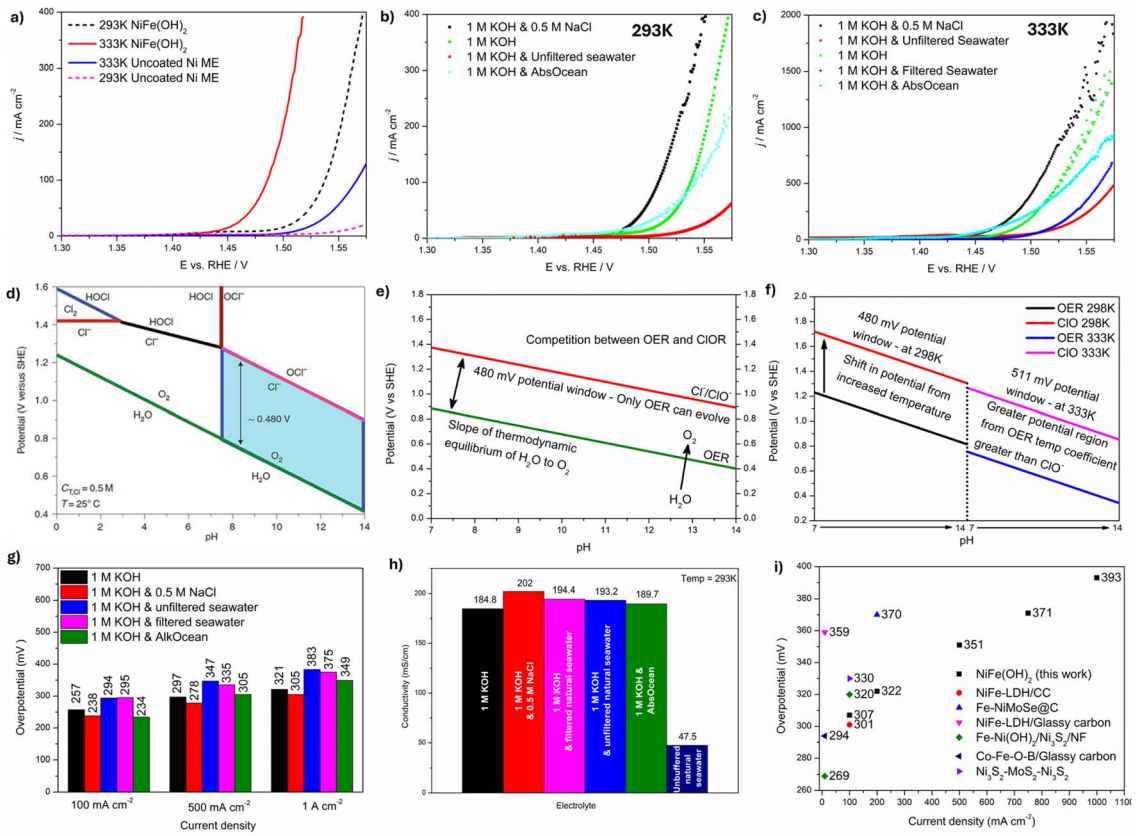

Fig. 5 (a) LSVs of catalyst-coated Ni microelectrode in 1 KOH at 293 K and 333 K and $NiFe(OH)_2$ coated microelectrode *vs.* pristine Ni microelectrode in 1 KOH at 333 K at a scan rate of 1 mV s^{-1} (b) LSV curves of $NiFe(OH)_2$ coated microelectrode in 1 M KOH *vs.* 1 M KOH & 0.5 M NaCl *vs.* 1 M KOH & unfiltered seawater *vs.* 1 M KOH & filtered seawater *vs.* 1 M KOH & Alk-AbsOcean at 293 K at a scan rate of 1 mV s^{-1} (c) LSV curves of $NiFe(OH)_2$ coated microelectrode in 1 M KOH *vs.* 1 M KOH & 0.5 M NaCl *vs.* 1 M KOH & unfiltered seawater *vs.* 1 M KOH & filtered seawater *vs.* 1 M KOH & Alk-AbsOcean at 333 K at a scan rate of 1 mV s^{-1} (d) Pourbaix diagram for NaCl with a concentration of 0.5 M[79] (e) maximum permitted overpotentials for OER electrocatalysts at 298 K (f) modified Pourbaix diagram to show the effect of elevated temperature (g) overpotentials recorded for $NiFe(OH)_2$ in varying electrolytes at 333 K (h) conductivity of electrolytes tested within the study at 293 K (i) comparison of $NiFe(OH)_2$ to similarly reported OER electrocatalysts in simulated seawater at ambient/room temperature.

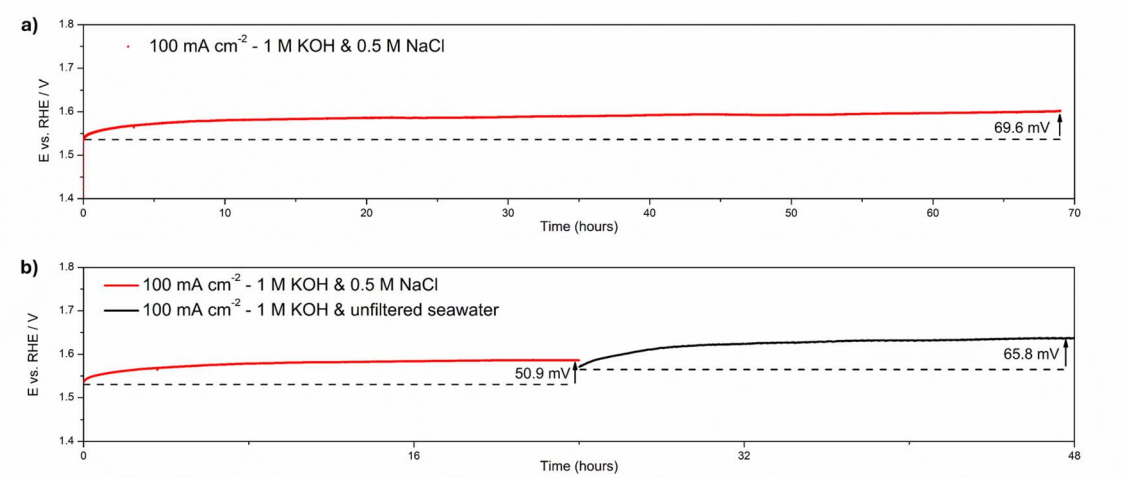

Fig. 6 (a) CP stability test in 1 M KOH & 0.5 M NaCl at 293 K at a constant current of 100 mA cm^{-2} for 70 hours using $NiFe(OH)_2$ coated at 250 mA cm^{-2} on a Ni microelectrode (b) comparison of $NiFe(OH)_2$ at a constant current of 100 mA cm^{-2} in 1 M KOH & 0.5 M NaCl and 1 M KOH & unfiltered seawater at 293 K on a Ni microelectrode, tests were conducted separately with a new sample made for each experiment.

a current density of 0.1 mA cm^{-2}.[80] The $NiFe(OH)_2$ only required an overpotential of ~202 mV to reach 100 mA cm^{-2}, whereas the pristine microelectrode required ~337 mV. The increased performance is achieved due to the catalyst coating, increasing the conductivity and catalytic activity over the pristine microelectrode. Moreover, the catalyst coating increases the electrochemical surface area by approximately 57% and enhances the R_f value, which facilitates better mass transport since the unevenness and porosity improve the diffusion and removal of reactants and products (O_2) (Section 3.2). Remarkably, to reach current densities of 1000 and 2000 mA cm^{-2}, the $NiFe(OH)_2$ coated microelectrode requires an overpotential of 323 and 367 mV at 333 K, respectively (Table S4). Furthermore, the peak current density achieved by the catalyst during testing was 2500 mA cm^{-2} at 392 mV at 333 K. While the exact role of the catalytic activity is difficult to prove, we attribute the excellent performance of $NiFe(OH)_2$ to the combined effect of Ni and Fe, rather than using pure Ni or Fe oxide.[17,22–24] Specifically, it is hypothesised that the incorporation of Fe^{3+} (Fig. 3c), changes the thermodynamics of the catalyst. The addition of Fe, increases the difficultly for Ni to undergo phase transformation prior to the OER (Ni^{2+} to Ni^{3+}) as Fe^{3+} stabilises the active Ni^{2+} ions from getting oxidised further which was supported by the delayed anodic shift of $Ni(OH)_2 \rightarrow NiOOH$ oxidation peak with the reduced integrated charge.[29,81] This is further confirmed by the XPS spectra highlights the significant contribution of Ni^{2+} within the sample, even post electrolysis (Fig. 7g).

3.5.2. 1 M KOH & 0.5 M NaCl (alkaline simulated seawater). Fig. 5c compares the $NiFe(OH)_2$ tested in 1 M KOH + 0.5 M NaCl *vs.* 1 M KOH at 333 K with a scan rate of 1 mV s^{-1} to achieve near-steady-state conditions. Introducing NaCl into the solution presents a competing reaction with the OER in alkaline media. This means that while the OER is thermodynamically favoured due to a lower equilibrium potential (1.23 V *vs.* reversible hydrogen electrode, RHE) than the chlorine evolution reaction (ClER) (1.36 V *vs.* RHE, pH 0) under standard conditions.[82,83] The ClER is the predominant anodic reaction within acidic mediums. However, the ClER has faster kinetics as a 2-electron oxidation reaction, compared to the 4-electron process of the sluggish OER involving 4 electrons.[12] Still, the ClER equilibrium potential is not dependent on pH, unlike the OER equilibrium potential, which can be influenced by pH (Fig. 5d).[82–84] Under alkaline conditions, Cl^- is oxidised to ClO^-, known as the chlorine oxidation reaction (ClOR).[83–86] ClOR is kinetically favoured over the OER under basic conditions, but the OER is more thermodynamically favourable.[82,84] The hypochlorite standard redox potential is heavily influenced by pH; the slope of pH dependency is identical to the slope of OER potential in the Pourbaix diagram under standard conditions (Fig. 5d).[82] The overpotential (η) for the ClOR is ~480 mV (1.72–1.23 = ~0.48 V), higher than that of OER in alkaline solutions of pH = 14.[17] Thus, if the anode operates at an overpotential of less than 480 mV in alkaline electrolytes, theoretically no hypochlorite will be formed as it is thermodynamically suppressed, and 100% OER selectivity can be achieved.[12,83] As a result, an ideal operating region is proposed for selective OER control, where the overpotential must be smaller than 480 mV at a pH greater than 7.5 at room temperature (Fig. 5d–f).[82]

At ~100 mA cm^{-2}, there is a reduction in overpotential of 18 mV compared to the KOH electrolyte. The results are in accordance with recently reported literature in that the addition of NaCl does not decrease the performance of electrocatalysts, as would be expected from the high chloride concentration, accelerating localised corrosion of catalysts; instead, a performance improvement is observed due to the increased ionic conductivity (Fig. 5h) (202 mS cm^{-1} and 184.8 mS cm^{-1} for 1 M KOH/NaCl and 1 M KOH, respectively).[15,84,87–91] This assumes that the absence of the ClOR occurs due to operating in potential regions <480 mV. Building upon this point, further investigation was conducted on the 480 mV threshold to trigger the ClOR and below.

While this theoretical limit could be argued as an oversimplification and unreasonable due to the assumption of

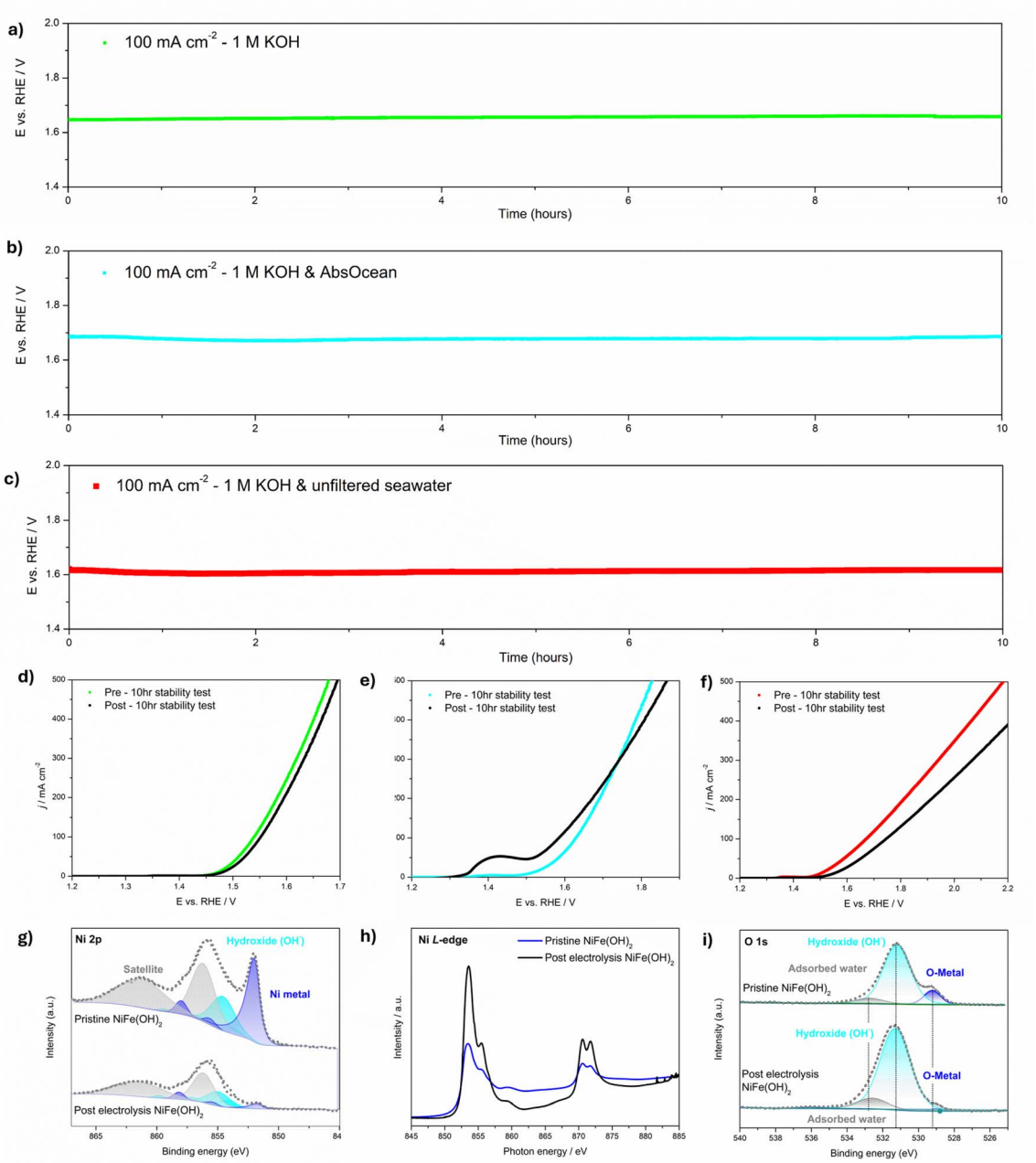

Fig. 7 CP stability test at 293 K at a constant current of 100 mA cm^{-2} for 10 hours using $NiFe(OH)_2$ coated at 25 mA cm^{-2} on a Ni foam (a) in 1 M KOH (b) in 1 M KOH & AbsOcean (c) in 1 M KOH & unfiltered seawater. LSVs of $NiFe(OH)_2$ before and after 10 h stability test with 80% *iR* compensation applied (d) in 1 M KOH (e) in 1 M KOH & AbsOcean (f) in 1 M KOH & unfiltered seawater (g) XPS spectrum of $NiFe(OH)_2$ in the Ni 2p region, pristine and post electrolysis at 50 mA cm^{-2} for 4 hours in 1 M KOH & AbsOcean (h) normalised Ni L-edge XANES spectra for $NiFe(OH)_2$ on carbon plate pristine and post electrolysis (i) XPS spectrum of $NiFe(OH)_2$ in the O 1s region, pristine and post electrolysis.

working under ideal conditions, if the potential is insufficient to trigger ClOR, no hypochlorite can be created. Existing Pourbaix diagrams assume standard conditions, including temperature and pressure (Fig. 5d). We caution against using certain thermodynamic potential thresholds (480 mV) at higher temperatures (Fig. 5e), as it is well known that increasing temperatures accelerates reaction kinetics, reducing overpotentials required to reach higher current densities. Therefore, we calculate a temperature coefficient for OER and ClOR at elevated temperatures.[92] The results indicate (supporting information, eqn (S1)–(S7)) that the OER temperature coefficient (−1.682 mV K^{-1}) is greater than ClOR (−1.08 mV K^{-1}), meaning that onset potential decreases at a faster rate for the OER over ClOR, suggesting that the thermodynamic potential gap increases at 333 K from 480 mV to 511 mV (eqn (S7)) despite increasing kinetics of generating ClOR. We propose a modified operating region based on temperature to reflect this (Fig. 5f), which is also supported by Horner *et al.*[93]

Notably, the $NiFe(OH)_2$ coated ME, illustrates great OER activity in alkaline simulated seawater compared with the

pristine Ni microelectrode even in 1 M KOH over the period of electrochemical testing. To deliver a current density of 100 mA cm^{-2}, the required overpotential for the $NiFe(OH)_2$ coated microelectrode and pristine Ni microelectrode are 238 mV and 336 mV, respectively (Fig. 5g). Fig. 5i illustrates the competitiveness of $NiFe(OH)_2$ in alkaline simulated seawater compared to similarly reported OER electrocatalysts, with one of the lowest overpotentials at 100 mA cm^{-2} and 250 mA cm^{-2}; while it is appreciated that the comparable studies are not recorded on a microelectrode, it is argued that many studies apply *iR* compensation to the recorded potentials, typically in the range of 80–90%, which is a similar way of reducing influence from *iR* drop in the system; thus, our comparison is still valid. Current densities exceeding 1000 mA cm^{-2} are less commonly reported, making our overpotential values difficult to compare. However, in Table S4, recent performance values from key literature, such as Cr_2O_3–CoO_x, which requires 420 mV to achieve 100 mA cm^{-2} in neutral seawater and S–Cu_2O–CuO, which requires 420 mV to achieve 500 mA cm^{-2}, contextualising the competitiveness of $NiFe(OH)_2$.[94,95] More recently, Du *et al.* presented state-of-the-art research in seawater electrolysis, utilising a corrosion-resistant NiFe layered double hydroxide electrode that achieves 1000 mA cm^{-2} at 200 mV and 220 mV in 1 M KOH & 0.5 M NaCl, respectively, and in 1 M KOH & natural seawater, but no specific *iR* compensation is provided.[96]

Notably, to achieve a current density of 1000 and 2000 mA cm^{-2}, the $NiFe(OH)_2$ coated microelectrode requires overpotentials of 305 and 341 mV at 333 K, respectively (Table S4). This is significantly lower than the theoretical ClOR threshold of 480 mV, indicating that theoretically, no ClO^- evolved during the electrochemical tests on the ME.

3.5.3. 1 M KOH & natural unfiltered & filtered seawater. We further tested the $NiFe(OH)_2$ coated microelectrode in 1 M KOH/unfiltered natural seawater, and 1 M KOH/filtered natural seawater to investigate the electrochemical performance in seawater environment, which has more complex composition. For instance, other ions, such as Ca^{2+}, Mg^{2+}, Br^- *etc.*, are not considered in the alkaline simulated seawater (1 M KOH & 0.5 M NaCl) solution.

Fig. 5b and c show the $NiFe(OH)_2$ tested in 1 M KOH and natural unfiltered seawater collected from Falmouth Bay, UK (50.1342° N, 5.0585° W). The $NiFe(OH)_2$ catalyst exhibits good OER performance in the alkaline unfiltered seawater electrolyte, but there is a noticeable decline compared to alkaline simulated seawater. To highlight this, to deliver a current density of 100 mA cm^{-2} in alkaline unfiltered seawater, the overpotential required is 294 mV (Fig. 5g). In comparison, to deliver a current density of 100 mA cm^{-2} in alkaline simulated seawater, the overpotential required is 238 mV (Fig. 5g). The decline in catalytic activity using alkaline unfiltered seawater could be due to pollutants and contaminants in seawater not present in the synthetic seawater electrolyte. The seawater's bacteria, microbes, and particulates may contaminate the electrode and block active sites, reducing OER performance; this phenomenon is well documented in seawater electrolysis literature.[90] A simple mechanical filtration system was used to pass the collected seawater to mitigate any contamination from solids such as sand or non-dissolved pollutants in the seawater. A finer level of filtration wasn't conducted since it defeats the objective of direct seawater electrolysis. In the alkaline filtered natural seawater electrolyte, to deliver a current density of 100 mA cm^{-2}, the overpotential required is 295 mV. Filtering the seawater before the electrochemical tests led to a 7 mV reduction at 100 mA cm^{-2} using the filtered seawater, compared to the unfiltered sample (Fig. 5c). The performance in the natural seawater electrolyte is comparable to and slightly better than the highly efficient NiFe-LDH/CC reported by Dong's group.[4,14] Furthermore, our results significantly outperform the Ni/Fe/Mo (oxy)hydroxides (OOH) presented by Xu's group, which required 330 mV to achieve 100 mA cm^{-2} (Table S4).[4,97] Moreover, the synthesis of this catalyst is significantly simpler than that of other reported OER electrocatalysts, which is a factor typically not considered when evaluating electrocatalysts. Our approach outperforms many non-precious metal OER electrocatalysts for seawater electrolysis, demonstrating its potential for achieving superior results in the field.

More importantly, the $NiFe(OH)_2$ can achieve current densities of 500 and 1000 mA cm^{-2} at 347 and 383 mV overpotentials, respectively, in 1 M KOH and unfiltered natural seawater. This is significantly lower than the 480 mV ClOR threshold, avoiding the Cl^- oxidation due to insufficient potential to evolve ClO^-.

3.5.4. 1 M KOH & Absolute Ocean (AbsOcean) standardised seawater. While using natural seawater, comparing datasets becomes complex due to geographical and seasonal variations in natural seawater composition and contamination levels. To this end, we introduced a standardised, commercially available seawater concentrate composition (Absolute Ocean (AbsOcean)) that is a more comprehensive seawater electrolyte compared to the simulated seawater.

Fig. 5b and c report the $NiFe(OH)_2$ catalyst within a buffered/alkaline AbsOcean electrolyte (1 M KOH & AbsOcean). $NiFe(OH)_2$ shows better performance in the AbsOcean electrolyte, compared to the natural seawater electrolytes (Fig. 5b and c), despite having a lower conductivity. This is likely due to AbsOcean having no bacteria and unknown particulate contaminants that occur in natural seawater samples; these contaminants are difficult to quantify and, because of this, complicate the anodic reaction. Despite this, the $NiFe(OH)_2$ performs well in the AbsOcean solution, reaching 100 mA cm^{-2} at overpotentials of 234 mV. The test was further conducted at room temperature for direct comparison with reported results. The catalytic performance of $NiFe(OH)_2$ at room temperature is also superior to most catalysts in literature, requiring only 311, 386 and 427 mV to reach current densities of 100, 500 and 1000 mA cm^{-2}. We suggest using AbsOcean standardised seawater to replace 1 M KOH and 0.5 M NaCl for better comparison between studies.

Furthermore, the $NiFe(OH)_2$ can achieve current densities of 1000 and 2000 mA cm^{-2} at 349 and 409 mV overpotentials, respectively, in 1 M KOH & AbsOcean.

3.6. Stability investigation of $NiFe(OH)_2$ in varying saline electrolytes

In addition to catalytic performance, long-term stability is a crucial parameter for OER electrocatalysts.

Chronopotentiometry (CP) is more representative of the realistic operation of an electrolyser than LSV, as it shows the impact of the generation and removal of the bubbles over an extended period of time. To this end, we investigated the stability of $NiFe(OH)_2$ by performing a range of tests using CP at different current densities in different alkaline seawater conditions in the three-electrode setup to avoid membrane complications from anions in seawater in a full anion exchange membrane cell presented in Fig. 6.

The OER long-term stability in alkaline simulated seawater was investigated at 100 mA cm^{-2}, and at room temperature to avoid electrolyte evaporation. Over a 70 hours period, the potential increased by 69.6 mV (Fig. 6a), indicating an approximately 0.99 mV h^{-1} degradation rate, with the majority of the potential increase stemming from the initial 10 hours of the test, most likely related to the activation and stabilisation of the catalyst as it undergoes surface changes or reconstruction to expose active sites, over time, the surface composition will stabilise, resulting in a more consistent potential. Following this, the catalyst begins to deteriorate steadily, as evidenced by the continuous increase in potential up to the 70 hours mark. Despite this, a degradation rate of 0.99 mV h^{-1} is comparable to similar reported OER electrocatalysts for DSWE and the overpotential during the test remains well below the 480 mV ClOR threshold.[90,98]

Moreover, Fig. 6b reveals the stability of $NiFe(OH)_2$ in 1 M KOH and 0.5 M NaCl *vs.* 1 M KOH and unfiltered seawater at 100 mA cm^{-2}. Over the period, the NaCl-containing electrolyte exhibited a degradation rate of 2.12 mV h^{-1}, compared to 2.74 mV h^{-1} in the seawater-containing electrolyte. While the seawater-containing electrolyte suffers reduced conductivity compared to NaCl-containing electrolyte (193.2 *vs.* 202 mS cm^{-1}), partially contributing to the higher overpotential, we also assume that the charge transfer overpotential is greater for the seawater electrolyte as the lower conductivity translates to fewer available charge carriers, which can slow down electron transfer kinetics.

The slow increase in potential is also likely attributed to some poisoning effect of the impurities within seawater, deactivating active sites of the catalyst, which are likely to have subtle surface effects rather than visible corrosion compared to the standardised alkaline simulated seawater solution. In essence, the combination of natural seawater's complex chemical composition, impurities, and microbial influences can all contribute to faster degradation of the OER electrocatalyst. Even below the hypochlorite potential, these factors collectively create a harsher environment for the catalyst than the simpler simulated seawater setup. In comparison, Lu *et al.* synthesised a NiFe-LDH/CC and tested within a KOH & seawater electrolytes, reporting 140 mV and 220 mV overpotentials over a 10 h period at 100 mA cm^{-2}, indicating degradation rates of 14 mV h^{-1} and 22 mV h^{-1}, respectively, demonstrating that $NiFe(OH)_2$ is more stable.

A further longer-term stability test was carried out on a Pt microelectrode to avoid any influence from the substrate; SEM analysis was conducted before and after the test. Fig. S9 shows a $NiFe(OH)_2$ coated Pt microelectrode in 1 M KOH and unfiltered seawater at 250 mA cm^{-2}. In full-cell scenarios, where flowing electrolytes facilitate bubble removal. Microbubbles generated on the microelectrode are more challenging to eliminate, contributing to higher overpotentials. In Fig. S9, the curve becomes noisier and generally displays a linearly increasing overpotential. This phenomenon occurs due to an accelerated rate of bubble formation, which obstructs the active sites on the electrode, thereby impacting the system's resistance and resulting in larger overpotentials. Over the 7.5 hours period, the potential increases by 111.3 mV, indicating a 14.84 mV h^{-1} degradation rate, and the potential exceeded the 1.72 V *vs.* RHE for the ClOR. Despite this, SEM analysis revealed no dramatic changes to the morphology of the catalyst after the test (Fig. S9a and b).

The catalyst was deposited at 25 mA cm^{-2} on Ni foam and held at 100 mA cm^{-2} in varying electrolytes at 293 K (Fig. 7). SEM and EDS analysis was conducted before and after testing (Fig. 7d–f) (Fig. S10–S15 and Table S3). As a result of the much larger electrode area, the benefits of using a microelectrode are no longer in place, giving rise to a significant *iR* drop within the setup; as the current flows through the solution, there is a greater amount of ionic resistance between the WE and the CE. To counter this, 80% *iR* compensation is applied to the dataset in Fig. 7.

Across Fig. 7a–c, the operating durability of $NiFe(OH)_2$ on Ni foam at 100 mA cm^{-2} remains stable with negligible rise in potential over 10 hours. Degradation rates of 1.02 mV h^{-1}, 1.3 mV h^{-1} and 1.6 mV h^{-1} are observed for Fig. 7a–c, respectively, highlight a linear degradation based on the electrolyte. Furthermore, after all 10 h tests (Fig. 7d–f) aspects of catalyst degradation are observed, with an increase in overpotential at higher current densities. After 10 hours at 100 mA cm^{-2}, to achieve 250 mA cm^{-2} in 1 M KOH requires 385 mV, whereas the pre-stability test samples, requires only 371 mV. In the saline electrolytes (Fig. 7e and f), 1 M KOH & AbsOcean and 1 M KOH & unfiltered seawater, to achieve 250 mA cm^{-2} after 10 hours, requires 532 and 707 mV, respectively. Whereas pre-stability test samples require 486 and 630 mV, respectively. Indicating the potential is within the region where hypochlorite can occur (>480 mV). Fig. 7 highlights significant catalyst degradation post-stability test leads us to attribute this decay to catalyst shedding from the substrate, resulting in a decline in the active catalyst surface area that participates in the reaction; however, further investigation is required to confirm this.

To get further insight to the degradation Fig. S11 explores the morphology change of $NiFe(OH)_2$ coated Ni foam before and after testing. Fig. S11a shows a pristine $NiFe(OH)_2$, highlighting a consistent catalyst coating and uniform morphology. Fig. S11b reveals the catalyst coating after 10 hours of testing in 100 mA cm^{-2}, the morphology remains mostly consistent with the pristine sample, no drastic change in morphology; the roughness appears similar, and groups of deposits are still evenly distributed across the surface. There are some minor elements of catalyst removal/peeling on the surface strands of the Ni foam, highlighting the that catalyst instability is stemming from mechanical instability between the coating and the substrate, likely leading to the performance degradation in

Fig. 7d–f. It is also consistent with the lower Fe EDS content and a higher Ni EDS content (Table S3), from the greater exposed substrate surface area. The XRD pattern in Fig. S17 confirms that post-electrolysis samples exhibit matching peak locations as a pristine sample; however, while the high-intensity peaks of the coated Ni substrate pattern at 44.5° and 52° correlate to metallic Ni stemming from the substrate, the peak intensity at 52° diminishes with respect to the peak at 44.5° in the pristine sample, as metallic Fe can be found to overlap with the peak at 52°, we attribute this intensity shift as a result of the loss of Fe in the sample.

In the saline electrolytes, (Fig. S11c–f), SEM analysis reveals a much more drastic morpholgy change over the pristine sample. In 1 M KOH & AbsOcean, performance degradation is observed (Fig. 7e), based on SEM analysis, we hypothesise that this degradation stems from the catalyst peeling from the substrate, and subsequent Cl^- ions corroding the substrate underneath, this can be illustrated in Fig. S14 and S15, where corrosion has occurred at an exposed area of substrate rather than pitting through the catalyst layer. In Fig. S15, the catalyst coating largely remains homogeneous, while the corroded area shows catalyst layer peeling at the edges, with the corroded area lacking catalyst entirely, which is hypothesised to have detached prior to the corrosion; catalyst detachment results from mechanical stress between the catalyst and substrate. Once detached, the exposed substrate can lead to localised potential accumulation and thus aiding the adsorption of Cl^- ions, accelerating eqn (13). This is confirmed by SEM and EDS analysis at areas where the catalyst layer appears to have peeled from the substrate, only Ni and Cl^- are observed on the spectra (Fig. S13b and S15). This trend is further observed in the 1 M KOH & unfiltered seawater electrolyte (Fig. S11e and f). Another factor affecting this is the other peaks observed in Fig. S16 post seawater electrolysis; there is more background noise observed in the post-electrolysis sample, with peaks attributed to chlorine, calcium and potassium, which will be residual left on the sample after seawater electrolysis, but it is also likely that some of this chlorine will be the adsorbed chloride from the electrolyte due to operating within the potential region to trigger the $ClOR^-$. It is believed that Cl^- adsorption follows this mechanism as reported in the literature:[99]

Adsorption:

$$M + Cl^- \rightarrow MCl_{ads} + e^- \rightarrow Ni + Cl^- \rightarrow NiCl_{ads} + e^- \quad (11)$$

Dissolution:

$$MCl_{ads} + Cl^- \rightarrow MCl_x^- \rightarrow NiCl_{ads} + Cl^- \rightarrow NiCl_x^- \quad (12)$$

Conversion:

$$MCl_x^- + OH^- \rightarrow M(OH)_x + Cl^- \rightarrow NiCl_x^- + OH^- \rightarrow Ni(OH)_x + Cl^- \quad (13)$$

Corrosion in the presence of Cl^- ions is attributed to three stages: adsorption, dissolution, and hydroxide formation or conversion. When the anodic potential is high, Cl^- ions can be readily adsorbed onto the positively polarised active surface. These anions then coordinate with the adsorbed ions, leading to dissolution (soluble chlorides) due to the adsorption and permeability of Cl^- ions. The formation of OH^- ions also speeds up hydroxide formation from the metal and chloride ions. To summarise, the corrosion mechanism comprises three reactions (eqn (11)–(13)). While theoretical, operating at a potential not sufficient to trigger ClO^- means that $NiFe(OH)_2$ proceeds solely through the OER mechanisms as described by Khalafallah *et al.*[100]

While the XRD pattern (Fig. S18) reveals some insight into this mechanism, it is difficult to distinguish between $Ni(OH)_2$ from the catalyst material, which is largely amorphous and that produced by the corrosion mechanism above. Insights into the surface chemistry is highlighted in Fig. 7g and h and reveal that the catalyst chemistry changes during seawater electrolysis, the contribution from Ni metal in the deposition process diminishes significantly (62.02% to 21.5%) while the $Ni(OH)_2$ increases to 78.50%, from 37.98%. The soft XAS spectra of Ni L-edge (Fig. 7h) highlight a similar effect; the peak shape remains consistent with the pristine samples, with more defined features, owing to the increase in Ni^{2+} within the sample, consistent with the greater contribution from $Ni(OH)_2$. The lack of a line shape change that would be expected of Ni^{2+} to Ni^{3+} confirms our earlier hypothesis that the addition of Fe increases the difficulty for Ni to undergo phase transformation before the OER (Ni^{2+} to Ni^{3+}) as Fe^{3+} stabilises the active Ni^{2+} ions from getting oxidised.[29,81] The lack of line shape variation persists with the Fe K-edge in Fig. S19, with the diminished intensity related to the loss of Fe content, consistent with our earlier analysis. In Fig. 7i, the ratio of the O 1s components changes from 1.5 : 10 : 1 in the pristine sample to 2 : 1 hydroxide to adsorbed water, consistent with the Ni L-edge results. The difficulty with specifying the origin of this mechanism is that it could be argued that it is impacted by the oxidation of the catalyst in alkaline environments.

4 Conclusion

In this work, a highly effective and low-cost OER electrocatalyst that is fast and simple to synthesise has been investigated in a range of seawater electrolytes using a microelectrode setup. The catalyst shows excellent OER performance in saline electrolytes, needing only 278 and 305 mV in alkaline simulated seawater as well as 347 and 383 mV in alkaline natural unfiltered seawater to achieve 500 and 1000 mA cm^{-2}, respectively. Substantial current densities >2000 mA cm^{-2} in 1 M KOH and alkaline simulated seawater, 1 M KOH and AbsOcean are achieved while limiting the overpotential to below 480 mV. $NiFe(OH)_2$ has shown great potential in seawater electrolysis. To our knowledge, this study achieves some of the best results in a saline electrolyte for an OER electrocatalyst within a three-electrode setup without *iR* compensation. Furthermore, we have presented a revised kinetic consideration for operating at elevated temperatures, increasing the ClOR threshold from 480 mV to 511 mV, which is vital to simulate industrial conditions in saline electrolytes. The observed degradation rates (1.3 mV h^{-1} and 1.6 mV h^{-1} in 1 M KOH & 0.5 M NaCl and 1 M

KOH & AbsOcean, respectively) and morphological analysis provide valuable insights into the catalyst's operation within seawater electrolytes. These findings contribute to the understanding of green hydrogen generation using seawater and provide valuable information for designing highly active, durable electrocatalysts for water-splitting applications in the future. Further modifications, such as anionic/polyanionic doping or surface selective layers to the catalyst, could increase the corrosion resistance and stability and lead to a much better overall OER electrocatalyst.

Author contributions

J. Corbin: methodology, validation, formal analysis, investigation, data curation, visualization, and writing – original draft. X. Li: writing – review & editing, supervision, resources, project administration, funding acquisition, conceptualization. A. Graf: XPS data collection and partial analysis. D. Trudgeon, M. Jones, C. Lyu, Z. Zhang, A. Loh, J. Cao & I. Nawrocka: writing – review & editing.

Conflicts of interest

The authors declare no conflict of interest.

Data availability

The data supporting this article have been included as part of the Supplementary Information (SI). The raw data supporting the findings of this research are available from the corresponding author upon reasonable request. Supplementary information is available. See DOI: https://doi.org/10.1039/d5su00650c.

Acknowledgements

Jack Corbin would like to acknowledge the PhD studentship awarded by the University of Exeter. The authors would like to acknowledge the funding support from the European Union's Horizon 2020 research and innovation programme under grant agreement No. 875524, the Interreg 2 Seas programme 2014–2020 co-funded by the European Regional Development Fund under subsidy contract No. 2S03-019, the EPSRC Supergen Energy Storage Project (grant number: EP/P003494/1), and the Royal Academy of Engineering through the UK-Germany Energy Systems Symposium of Engineering UK-Germany Energy Systems Symposium Award (UKDE\100005). The X-ray photoelectron (XPS) data collection was performed at the EPSRC National Facility for XPS ("HarwellXPS"), operated by Cardiff University and UCL, under Contract No. PR16195. For the purpose of open access, the author has applied a Creative Commons Attribution (CCBY) licence to any Author Accepted Manuscript version arising from this submission.

References

1 C. Wang, H. Shang, L. Jin, H. Xu and Y. Du, *Nanoscale*, 2021, **13**, 7897–7912.
2 World Nuclear Association, *Heat Values of Various Fuels*, https://world-nuclear.org/information-library/facts-and-figures/heat-values-of-various-fuels.aspx, accessed 4 January 2023.
3 Y. Kuang, M. J. Kenney, Y. Meng, W.-H. Hung, Y. Liu, J. E. Huang, R. Prasanna, P. Li, Y. Li, L. Wang, M.-C. Lin, M. D. McGehee, X. Sun and H. Dai, *Proc. Natl. Acad. Sci. U. S. A.*, 2019, **116**, 6624–6629.
4 J. Corbin, M. Jones, C. Lyu, A. Loh, Z. Zhang, Y. Zhu and X. Li, *RSC Adv.*, 2024, **14**, 6416–6442.
5 D. Khalafallah, F. Qiao, C. Liu, J. Wang, Y. Zhang, J. Wang, Q. Zhang and P. H. L. Notten, *Coord. Chem. Rev.*, 2023, **496**, 215405.
6 L. Yu, J. Xiao, C. Huang, J. Zhou, M. Qiu, Y. Yu, Z. Ren, C.-W. Chu and J. C. Yu, *Proc. Natl. Acad. Sci. U. S. A.*, 2022, **119**(18), e2202382119.
7 R. Vinodh, T. Palanivel, S. S. Kalanur and B. G. Pollet, *Energy Adv.*, 2024, **3**, 1144–1166.
8 M. Jones, C. Lyu, D. Trudgeon, J. Corbin, I. Nawrocka, Z. Zhang, M. B. Lykkegaard, S. Guan, T. Dodwell and X. Li, *Mater. Today Chem.*, 2024, **42**, 102414.
9 L. Wu, L. Yu, X. Xiao, F. Zhang, S. Song, S. Chen and Z. Ren, *Research*, 2020, **2020**, 3976278.
10 F. Dionigi, Z. Zeng, I. Sinev, T. Merzdorf, S. Deshpande, M. B. Lopez, S. Kunze, I. Zegkinoglou, H. Sarodnik, D. Fan, A. Bergmann, J. Drnec, J. F. de Araujo, M. Gliech, D. Teschner, J. Zhu, W.-X. Li, J. Greeley, B. R. Cuenya and P. Strasser, *Nat. Commun.*, 2020, **11**, 2522.
11 Z.-S. Wu, G. Zhou, L.-C. Yin, W. Ren, F. Li and H.-M. Cheng, *Nano Energy*, 2012, **1**, 107–131.
12 M. Ning, F. Zhang, L. Wu, X. Xing, D. Wang, S. Song, Q. Zhou, L. Yu, J. Bao, S. Chen and Z. Ren, *Energy Environ. Sci.*, 2022, **15**, 3945–3957.
13 J. E. Park, S. Y. Kang, S.-H. Oh, J. K. Kim, M. S. Lim, C.-Y. Ahn, Y.-H. Cho and Y.-E. Sung, *Electrochim. Acta*, 2019, **295**, 99–106.
14 G. Dong, F. Xie, F. Kou, T. Chen, F. Wang, Y. Zhou, K. Wu, S. Du, M. Fang and J. C. Ho, *Mater. Today Energy*, 2021, **22**, 100883.
15 J. Lu, C. Li, H. Wang, S. Ji, X. Wang and R. Wang, *Int. J. Hydrogen Energy*, 2021, **46**, 12936–12943.
16 M. Ning, L. Wu, F. Zhang, D. Wang, S. Song, T. Tong, J. Bao, S. Chen, L. Yu and Z. Ren, *Mater. Today Phys.*, 2021, **19**, 100419.
17 I. Vincent, E.-C. Lee and H.-M. Kim, *Catalysts*, 2022, **12**, 476.
18 H. Osgood, S. V. Devaguptapu, H. Xu, J. Cho and G. Wu, *Nano Today*, 2016, **11**, 601–625.
19 N. Li, D. K. Bediako, R. G. Hadt, D. Hayes, T. J. Kempa, F. Von Cube, D. C. Bell, L. X. Chen and D. G. Nocera, *Proc. Natl. Acad. Sci. U. S. A.*, 2017, **114**, 1486–1491.
20 L. Trotochaud, S. L. Young, J. K. Ranney and S. W. Boettcher, *J. Am. Chem. Soc.*, 2014, **136**, 6744–6753.

21 S. Anantharaj, S. Kundu and S. Noda, *Nano Energy*, 2021, **80**, 105514.
22 D. Friebel, M. W. Louie, M. Bajdich, K. E. Sanwald, Y. Cai, A. M. Wise, M.-J. Cheng, D. Sokaras, T.-C. Weng, R. Alonso-Mori, R. C. Davis, J. R. Bargar, J. K. Nørskov, A. Nilsson and A. T. Bell, *J. Am. Chem. Soc.*, 2015, **137**, 1305–1313.
23 C. Liang, P. Zou, A. Nairan, Y. Zhang, J. Liu, K. Liu, S. Hu, F. Kang, H. J. Fan and C. Yang, *Energy Environ. Sci.*, 2020, **13**, 86–95.
24 L. Wang, X. Ge, Y. Li, J. Liu, L. Huang, L. Feng and Y. Wang, *J. Mater. Chem. A*, 2017, **5**, 4331–4334.
25 F. Song, M. M. Busch, B. Lassalle-Kaiser, C.-S. Hsu, E. Petkucheva, M. Bensimon, H. M. Chen, C. Corminboeuf and X. Hu, *ACS Cent. Sci.*, 2019, **5**, 558–568.
26 I. Spanos, J. Masa, A. Zeradjanin and R. Schlögl, *Catal. Lett.*, 2021, **151**, 1843–1856.
27 B. Hunter, J. Winkler and H. Gray, *Molecules*, 2018, **23**, 903.
28 A. Loh, X. Li, O. O. Taiwo, F. Tariq, N. P. Brandon, P. Wang, K. Xu and B. Wang, *Int. J. Hydrogen Energy*, 2020, **45**, 24232–24247.
29 X. Li, F. C. Walsh and D. Pletcher, *Phys. Chem. Chem. Phys.*, 2011, **13**, 1162–1167.
30 H. Ullah, A. Loh, D. P. Trudgeon and X. Li, *ACS Omega*, 2020, **5**, 20517–20524.
31 C. Liang, P. Zou, A. Nairan, Y. Zhang, J. Liu, K. Liu, S. Hu, F. Kang, H. J. Fan and C. Yang, *Energy Environ. Sci.*, 2020, **13**, 86–95.
32 T. Haq and Y. Haik, *ACS Sustain. Chem. Eng.*, 2022, **10**, 6622–6632.
33 J. N. Hausmann, R. Schlögl, P. W. Menezes and M. Driess, *Energy Environ. Sci.*, 2021, **14**, 3679–3685.
34 W. G. Proud and C. Müller, *Electrochim. Acta*, 1993, **38**, 405–413.
35 R. Oriňáková, A. Turoňová, D. Kladeková, M. Gálová and R. M. Smith, *J. Appl. Electrochem.*, 2006, **36**, 957–972.
36 I. Epelboin, M. Joussellin and R. Wiart, *J. Electroanal. Chem. Interfacial Electrochem.*, 1981, **119**, 61–71.
37 J. O. Bockris, D. Drazic and A. R. Despic, *Electrochim. Acta*, 1961, **4**, 325–361.
38 G. A. Di Bari, in *Modern Electroplating*, Wiley, 2010, pp. 79–114.
39 Y. Wang, N. Williamson, R. Dawson and N. Bimbo, *J. Appl. Electrochem.*, 2023, **53**, 877–892.
40 A. Loh, *Development of Electrocatalysts for Oxygen Electrodes in Alkaline Electrochemical Systems*, 2019.
41 A. M. Rashidi and A. Amadeh, *Surf. Coat. Technol.*, 2008, **202**, 3772–3776.
42 L. Rocchetti, A. Amato and F. Beolchini, *J. Clean. Prod.*, 2016, **116**, 299–305.
43 N.-Y. Kang and J.-H. Lee, *Electron. Mater. Lett.*, 2023, **19**, 503–509.
44 H.-H. Huang, K. K. H. De Silva, G. R. A. Kumara and M. Yoshimura, *Sci. Rep.*, 2018, **8**, 6849.
45 Q. T. Ain, S. H. Haq, A. Alshammari, M. A. Al-Mutlaq and M. N. Anjum, *Beilstein J. Nanotechnol.*, 2019, **10**, 901–911.
46 F. Sun, J. Qin, Z. Wang, M. Yu, X. Wu, X. Sun and J. Qiu, *Nat. Commun.*, 2021, **12**, 4182.
47 J. Wang, P. Yang, X. Wei and Z. Zhou, *Nanoscale Res. Lett.*, 2015, **10**, 119.
48 Z. Wei, H. Qiao, H. Yang, C. Zhang and X. Yan, *J. Alloys Compd.*, 2009, **479**, 855–858.
49 F. Davar, Z. Fereshteh and M. Salavati-Niasari, *J. Alloys Compd.*, 2009, **476**, 797–801.
50 S. Akinkuade, B. Mwankemwa, J. Nel and W. Meyer, *Phys. B*, 2018, **535**, 24–28.
51 F. Dionigi and P. Strasser, *Adv. Energy Mater.*, 2016, **6**(23), 1614–6832.
52 S. Jung, R. A. Senthil, A. Min, A. Kumar, C. J. Moon, G. H. Jeong, T. W. Kim and M. Y. Choi, *J. Mater. Chem. A*, 2024, **12**, 8694–8706.
53 A. Seijas-Da Silva, A. Hartert, V. Oestreicher, J. Romero, C. Jaramillo-Hernández, L. J. J. Muris, G. Thorez, B. J. C. Vieira, G. Ducourthial, A. Fiocco, S. Legendre, C. Huck-Iriart, M. Mizrahi, D. López-Alcalá, A. T. S. Freiberg, K. J. J. Mayrhofer, J. C. Waerenborgh, J. J. Baldoví, S. Cherevko, M. Varela, S. Thiele, V. Lloret and G. Abellán, *Nat. Commun.*, 2025, **16**, 6138.
54 X. An, Q. Hu, W. Zhu, L. Liu, Y. Zhang and J. Zhao, *Appl. Phys. A*, 2021, **127**, 865.
55 S. Liu, H. Zhang, E. Hu, T. Zhu, C. Zhou, Y. Huang, M. Ling, X. Gao and Z. Lin, *J. Mater. Chem. A*, 2021, **9**, 23697–23702.
56 A. Zaffora, B. Megna, B. Seminara, F. Di Franco and M. Santamaria, *Nanomaterials*, 2024, **14**, 407.
57 J.-B. Wu, M.-L. Lin, X. Cong, H.-N. Liu and P.-H. Tan, *Chem. Soc. Rev.*, 2018, **47**, 1822–1873.
58 M. C. Biesinger, B. P. Payne, L. W. M. Lau, A. Gerson and R. St. C. Smart, *Surf. Interface Anal.*, 2009, **41**, 324–332.
59 C. Lyu, A. Loh, M. Jones, D. Trudgeon, J. Corbin, J. Cao, Z. Zhang, P. Connor and X. Li, Electrodeposition and Optimisation of Amorphous Ni_xS_y Catalyst for Hydrogen Evolution Reaction in Alkaline Environment., *Chem. – Euro. J.*, 2024, **30**(66), e202403030.
60 C. Mahala, M. Devi Sharma and M. Basu, *ChemElectroChem*, 2019, **6**, 3488–3498.
61 J. W. Pinder, G. H. Major, D. R. Baer, J. Terry, J. E. Whitten, J. Čechal, J. D. Crossman, A. J. Lizarbe, S. Jafari, C. D. Easton, J. Baltrusaitis, M. A. van Spronsen and M. R. Linford, *Appl. Surf. Sci. Adv.*, 2024, **19**, 100534.
62 Thermo Fisher Scientific Inc., *Iron X-ray photoelectron spectra*, https://www.thermofisher.com/uk/en/home/materials-science/learning-center/periodic-table/transition-metal/iron.html, accessed on 23 July 2025.
63 W. Wan, Y. Zhao, S. Wei, C. A. Triana, J. Li, A. Arcifa, C. S. Allen, R. Cao and G. R. Patzke, *Nat. Commun.*, 2021, **12**, 5589.
64 C. A. Hall, P. Ferrer, D. C. Grinter, S. Kumar, I. da Silva, J. Rubio-Zuazo, P. Bencok, F. de Groot, G. Held and R. Grau-Crespo, *J. Mater. Chem. A*, 2024, **12**, 29645–29656.
65 F. Lin, D. Nordlund, T. Pan, I. M. Markus, T.-C. Weng, H. L. Xin and M. M. Doeff, *J. Mater. Chem. A*, 2014, **2**, 19833–19840.

66 H. Wang, S. M. Butorin, A. T. Young and J. Guo, *J. Phys. Chem. C*, 2013, **117**, 24767–24772.
67 J. van Elp, B. G. Searle, G. A. Sawatzky and M. Sacchi, *Solid State Commun.*, 1991, **80**, 67–71.
68 H. Wang, C. Y. Ralston, D. S. Patil, R. M. Jones, W. Gu, M. Verhagen, M. Adams, P. Ge, C. Riordan, C. A. Marganian, P. Mascharak, J. Kovacs, C. G. Miller, T. J. Collins, S. Brooker, P. D. Croucher, K. Wang, E. I. Stiefel and S. P. Cramer, *J. Am. Chem. Soc.*, 2000, **122**, 10544–10552.
69 D. P. Trudgeon and X. Li, *Batteries*, 2022, **8**, 276.
70 C. Hitz and A. Lasia, *J. Electroanal. Chem.*, 2002, **532**, 133–140.
71 N. K. Shrestha, S. A. Patil, J. Han, S. Cho, A. I. Inamdar, H. Kim and H. Im, *J. Mater. Chem. A*, 2022, **10**, 8989–9000.
72 F. Lissandrello, N. Lecis and L. Magagnin, *Electrochim. Acta*, 2024, **478**, 143840.
73 A. Loh, X. Li, O. O. Taiwo, F. Tariq, N. P. Brandon, P. Wang, K. Xu and B. Wang, *Int. J. Hydrogen Energy*, 2020, **45**, 24232–24247.
74 M. E. G. Lyons and M. P. Brandon, *The Oxygen Evolution Reaction on Passive Oxide Covered Transition Metal Electrodes in Aqueous Alkaline Solution. Part 1-Nickel*, 2008, vol. 3.
75 M. E. G. Lyons and M. P. Brandon, *The Oxygen Evolution Reaction on Passive Oxide Covered Transition Metal Electrodes in Alkaline Solution Part II-Cobalt*, 2008, vol. 3.
76 I. García-López, L. F. Arenas, T. Turek, V. I. Águeda and A. Garrido-Escudero, *React. Chem. Eng.*, 2023, **8**, 1776–1784.
77 M. Fallah Vostakola, H. Ozcan, R. S. El-Emam and B. Amini Horri, *Energies*, 2023, **16**, 3327.
78 D. Ferrero, A. Lanzini, M. Santarelli and P. Leone, *Int. J. Hydrogen Energy*, 2013, **38**, 3523–3536.
79 S.-C. Ke, R. Chen, G.-H. Chen and X.-L. Ma, *Energy Fuels*, 2021, **35**, 12948–12956.
80 Q. Jiang, S. Wang, C. Zhang, Z. Sheng, H. Zhang, R. Feng, Y. Ni, X. Tang, Y. Gu, X. Zhou, S. Lee, D. Zhang and F. Song, *Nat. Commun.*, 2023, **14**, 6826.
81 S. Anantharaj, S. Kundu and S. Noda, *Nano Energy*, 2021, **80**, 105514.
82 S. Fukuzumi, Y.-M. Lee and W. Nam, *ChemSusChem*, 2017, **10**, 4264–4276.
83 Y. S. Park, J. Lee, M. J. Jang, J. Yang, J. Jeong, J. Park, Y. Kim, M. H. Seo, Z. Chen and S. M. Choi, *J. Mater. Chem. A*, 2021, **9**, 9586–9592.
84 F. Dionigi, T. Reier, Z. Pawolek, M. Gliech and P. Strasser, *ChemSusChem*, 2016, **9**, 962–972.
85 L. Yu, Q. Zhu, S. Song, B. McElhenny, D. Wang, C. Wu, Z. Qin, J. Bao, Y. Yu, S. Chen and Z. Ren, *Nat. Commun.*, 2019, **10**, 5106.
86 H. J. Song, H. Yoon, B. Ju, D.-Y. Lee and D.-W. Kim, *ACS Catal.*, 2020, **10**, 702–709.
87 P. Hajjar, M.-A. Lacour, N. Masquelez, J. Cambedouzou, S. Tingry, D. Cornu and Y. Holade, *Molecules*, 2021, **26**, 5926.
88 S. Dresp, F. Dionigi, S. Loos, J. Ferreira de Araujo, C. Spöri, M. Gliech, H. Dau and P. Strasser, *Adv. Energy Mater.*, 2018, **8**, 1800338.
89 S. Dresp, F. Dionigi, M. Klingenhof, T. Merzdorf, H. Schmies, J. Drnec, A. Poulain and P. Strasser, *ACS Catal.*, 2021, **11**, 6800–6809.
90 L. Yu, L. Wu, B. McElhenny, S. Song, D. Luo, F. Zhang, Y. Yu, S. Chen and Z. Ren, *Energy Environ. Sci.*, 2020, **13**, 3439–3446.
91 G. Amikam, P. Nativ and Y. Gendel, *Int. J. Hydrogen Energy*, 2018, **43**, 6504–6514.
92 S. G. Bratsch, *J. Phys. Chem. Ref. Data*, 1989, **18**, 1–21.
93 O. Horner, E. L. Gyenge and D. P. Wilkinson, *ECS Meeting Abstracts*, MA2024-01, 2024, pp. 1724.
94 J. Guo, Y. Zheng, Z. Hu, C. Zheng, J. Mao, K. Du, M. Jaroniec, S.-Z. Qiao and T. Ling, *Nat. Energy*, 2023, **8**, 264–272.
95 T. ul Haq and Y. Haik, *Catal. Today*, 2022, **400–401**, 14–25.
96 J Du, Z Li, L Wang, Y Ding, W Ye, W Yang and L Sun, *Advanced Science*, 2025, **12**(22), 202416661.
97 L. Xu, Y. Dong, W. Xu and W. Zhang, *Catalysts*, 2023, **13**, 924.
98 L. Wu, L. Yu, F. Zhang, B. McElhenny, D. Luo, A. Karim, S. Chen and Z. Ren, *Adv. Funct. Mater.*, 2020, **31**(1), 1616–3028.
99 S. Jung Kim, H. Choi, J. Ho Ryu, K. Min Kim, S. Mhin, A. Kumar Nayak, J. Bang, M. Je, G. Ali, K. Yoon Chung, K.-H. Na, W.-Y. Choi, S. Yeo, J. Uk Jang and H. Han, *J. Energy Chem.*, 2023, **81**, 82–92.
100 D. Khalafallah, L. Feng, Z. Sun, S. Tong, J. Wang and Q. Zhang, *Adv. Funct. Mater.*, 2025, 2506186.